Title

Coaxial Vacuum Gap Breakdown for Pulsed Power Liners

Author

Cordaro, Samuel

Publication Date

2018

UNIVERSITY OF CALIFORNIA SAN DIEGO

Coaxial Vacuum Gap Breakdown for Pulsed Power Liners

A Thesis submitted in partial satisfaction of the requirements for the degree Master of Science

in

Engineering Sciences (Engineering Physics)

by

Samuel Winget Cordaro

Committee in charge:

Sergei Krasheninnikov, Chair
Simon Bott-Suzuki
Christopher Holland
Jan Kleissl

2018

The Thesis of Samuel Winget Cordaro is approved, and it is acceptable in quality and form for publication on microfilm and electronically:

Chair

University of California San Diego

2018

DEDICATION

To my Family.

EPIGRAPH

"…we must become the best learners and discoverers of everything that is lawful and necessary in the world: we must become *physicists* in order to be able to be *creators* in this sense—while hitherto all valuations and ideals have been based on *ignorance* of physics or were constructed so as to *contradict* it. Therefore: long live physics! And even more so that which *compels* us to turn to physics—our honesty!"

—*Friedrich Nietzsche,* Die fröhliche Wissenschaft (The Gay Science)

TABLE OF CONTENTS

LIST OF FIGURES

LIST OF TABLES

ACKNOWLEDGEMENTS

I would like to thank Dr. Simon Bott-Suzuki for his support as my mentor and project advisor. Over the past few years, his guidance has proved to be invaluable to the success of this experiment, and to my growth as an experimental physicist. I would also like to thank Professor Sergei Krasheninnikov for his support as chair of my committee and academic advisor. I would also like to thank Dr. Christopher Holland and Professor Jan Kleissl for agreeing to sit on my committee.

Chapter 2, in part, a reprint of the material as it appears in “Two dimensional triangulation of breakdown in a high voltage coaxial gap” S.W. Cordaro, S. C. Bott-Suzuki, L.S. Caballero Bendixsen, in Review of Scientific Instruments, 86,073503 (2015). The thesis author was the primary investigator and author of this paper.

Chapter 3, in part, a reprint of the material as it appears in “Time and Space resolved current density mapping in three dimensions using magnetic field probe array in a high voltage coaxial gap” S.W. Cordaro, S. C. Bott-Suzuki, in the Journal of Applied Physics 122, 213303 (2017). The thesis author was the primary investigator and author of this paper.

Chapter 4, in part is currently being prepared for submission for publication of the material by S.W Cordaro and S.C Bott-Suzuki. The thesis author was the primary investigator and author of this material.

VITA

2013 Bachelor of Science, Applied Physics, Rensselaer Polytechnic Institute

2018 Master of Science, Engineering Sciences (Engineering Physics), University of California San Diego

Publications

“Two dimensional triangulation of breakdown in a high voltage coaxial gap”, S. W. Cordaro et al. Rev. Sci. Instrum. 86, 073503 (2015)

“Time and Space resolved current density mapping in three dimensions using magnetic field probe array in a high voltage coaxial gap” S. W. Cordaro and S. C. Bott-Suzuki J. Appl. Phys. 122, 213303 (2017)

Fields of Study

Major Field: Engineering Physics

Studies in Experimental Plasma Physics

Dr. Simon Bott-Suzuki

ABSTRACT OF THE THESIS

Coaxial Vacuum Gap Breakdown for Pulsed Power Liners

by

Samuel Winget Cordaro

Master of Science in Engineering Sciences (Engineering Physics)

University of California San Diego, 2018

Professor Sergei Krasheninnikov, Chair

Vacuum gap breakdown mechanisms for many geometries, such as sphere-sphere, plane-plane, and point-plane, are well understood and documented.[13] To date, no detailed analysis of a coaxial electrode geometry has been performed. This work is motivated by the need to better understand the mechanisms by which breakdown initiation occurs in a coaxial gap over a few

nanoseconds to a few microseconds at tens of kilo-volts over gap sizes up to 1.5 mm, especially considering how common the use of a coaxial gap is in high voltage power lines of large pulsed power machines.

Of specific interest is the evolution of the magnetic field in time and space along the gap and how asymmetries about the azimuth of this gap influence this evolution. Asymmetry in breakdown about the azimuth could be responsible for non-uniform distributions of voltage and current which could lead to early time scale instabilities of a load at the termination of a transmission line.

This work is relevant to larger pulsed power machines that presently make use of a µm high voltage coaxial vacuum gap in the power feed, such as the MagLIF [14] design on Sandia's Z-machine. On these larger machines, the cathode gap power feed cannot be observed and is usually not directly monitored by diagnostic tools. Often a direct observation of vacuum gaps is not feasible, a comprehensive method to observe and influence the evolution of the magnetic field and current density would prove beneficial.

Chapter 1: Background

1.1) Breakdown Theory: Field Emission

In field emission [1], electrons are drawn out of a metal surface by a high electrostatic field. It can be shown that at the surface of a metal electrode, a strong electric field can modify the potential barrier at that surface to such a level that electrons in an upper level close to the "Fermi" level will have a probability of passing through the barrier (vacuum). This passing through the barrier is known as a tunneling effect, and is experimentally seen as a breakdown, Figure 1. The electric fields required to produce such an effect are of order ~10^7 V/cm. Fields of this order are often seen at sharp points or surface irregularities of an electrode.

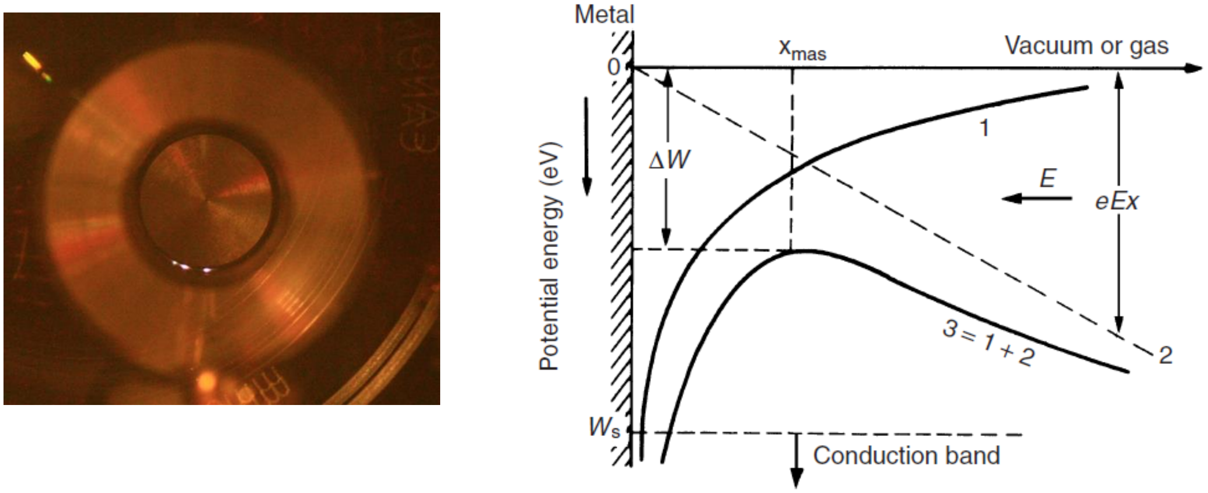

Figure 1: Experimental Breakdown emission in a coaxial gap (left), Breakdown emission diagram, which depicts the lowering of the potential barrier by an external electric field. The curve labeled 1 represents the energy of the system without a field, curve 2 represents the energy due to the field, and finally 3 represents the total energy of the system in the presence of the external electric field.

An expression for this breakdown emission can be derived if we consider a simple analytical model of a single electron moving from a metal plate in the +x^ direction, Figure 1. The electric field of such a system can be approximated as that of a point charge and an equipotential planar surface, which will denote our metal surface. Following convention we can see our field lines are the same as those when a test charge +q exists at a distance of (- x) on the opposite side of our metal surface. Thus by Coulomb's Law,

$$F(x) = -\frac{e^2}{4\pi\epsilon_0(2x)^2} \qquad (1.1)$$

And thus follows our, potential energy at any distance x is found as follows,

$$W_{e1} = \int_{\infty}^{x} F(x)dx = -\frac{e^2}{16\pi\epsilon_0 x} \qquad (1.2)$$

Equation 1.2 has been graphed on top of our Figure 2, which can be seen as a parabola. When the effect of the external field is applied at right angles to our metal surface (cathode surface), we can determine the potential energy given to the electron, which is as follows.

$$W_E = -eEx \qquad (1.3)$$

Again we graph this equation, on Figure 1, which is shown as a straight line. With this we can find the total energy of this system W_T;

$$W_T = W_{e1} + W_E \qquad (1.4)$$

This total energy, W_T , is also graphed on Figure 1, as a resultant curve of W_E and W_{e1}. We see that this is reduction ΔW results in a reduction of the barrier. The value at which W_{total} is maximized is found by determining where the gradient in the change in Work done/energy is zero thusly,

$$\frac{dW_T}{dx} = \frac{e^2}{16\pi\epsilon_0 x_{max}^2} - eE = 0$$

$$x_{max} = \sqrt{\frac{e}{16\pi\epsilon_0 E}}$$

$$W_T(x_{max}) = -e\sqrt{\frac{eE}{4\pi\epsilon_0}}$$

From this we find that the effective work function is as follows,

$$W_{eff} = W_s - W_T(x_{max}) \qquad (1.5)$$

W_s: The work function of the surface

At this point is it useful to begin determining the emission current density based on the effective work function (1.5). The emission/breakdown current is related to the temperature of the emitter as shown by the Richardson relation [2] for thermionically emitted saturation current density:

$$J_s = \frac{4\pi meK^2}{h^3} T^2 \exp\left[-\frac{W_s}{kT}\right] \qquad (1.6)$$

e,m: electron charge and mass

K: Boltzmann’s constant

T: Absolute temperature

W_s : Work function of the surface

Now we are able to combine our effective work function (1.5) and our current density equation (1.6) to find a modified current density due to electron emission.

$$J_s = \frac{4\pi meK^2}{h^3}T^2 \exp\left[-\frac{e}{kT}\left(W_s - \sqrt{\frac{eE}{4\pi\epsilon_0}}\right)\right]$$

Here we have arrived on a function that is dependent mainly on Temperature, Electric field, and the work function of the metal, this is known as the Schottky's equation[6]. For the experimental regime we are working in our temperature is room temperature, due to the fact that our current pulse is short (150ns) and our current and voltage relatively low (200-300 A, 25kV). So an emission current density equation that is based solely on the work function and the surface field is needed. This will be explored in the next section.

1.2) Cold Field Electron Emission

In 1928, Fowler and Nordheim derived a mathematical model that relates the applied electric field (F), the work function (ϕ) of the metal and the current density (J) of the emitted electrons [3] for a low temperature metal (~0 K). This derivation was closely related to work done by Oppenheimer [7] on the emission of electrons from the hydrogen atom influenced by high external electric field. The derivation is as follows.

In a similar way to the previous section, we first consider the emission through a potential energy barrier, Figure 2. Here the potential energy of electrons that will attempt to tunnel through a potential barrier are plotted. The dotted line is the assumed step function version of the potential energy of the electrons, with the curved line denoting a rounding of the potential energy at the sharp points due to the mirror image potential effect. Though it will be shown below that this rounding of the potential, which normally alters the emission coefficients significantly [6] for any non-zero external electric field with electrons whose incident energy is roughly equal to the kinetic energy of the electron motion normal to the emitter metal surface, is insignificant in strong field emission at room temperatures.

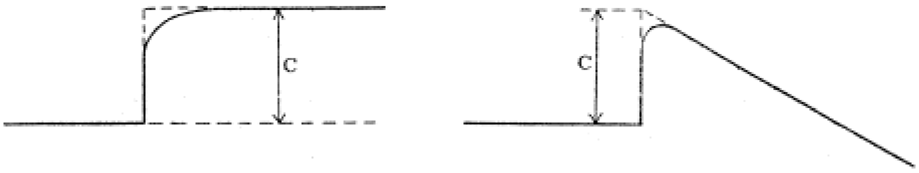

(i) (ii)

Figure 2: Potential barrier example

This is done by solving the wave equation through a potential energy step (dotted line) in Figure 2.

$$\frac{d^2}{dx^2}\Psi + \kappa^2(W - C + Fx)\Psi = 0 \qquad x > 0 \qquad (1)$$

$$\frac{d^2}{dx^2}\Psi + \kappa^2 W\Psi = 0 \qquad x < 0 \qquad (\mathbf{2})$$

Conditions: (1): Ψ & d Ψ/dx are continuous at x = 0

(2): x > 0 stream of electrons to the right only

$$\kappa^2 = 8\pi^2 m/h^2$$

At low temperatures nearly all the electrons are distributed such that W < C, so that we pass through a zero of the coefficient of ψ. Where W is the energy incident to the left on a surface, and C is the increase in potential energy. Thus,

$$\left(-\frac{C-W}{F}+x\right)(\kappa^2 F)^{\frac{1}{2}} = y$$

=> (1): $$\frac{d^2}{dx^2}\boldsymbol{\Psi} + \boldsymbol{y\Psi} = \mathbf{0}$$

This is just our basic wave equation which has solutions in terms of Bessel functions (O 1/3)[8]

$$\psi = \sqrt{y}J_{\pm\frac{1}{3}}\left(\frac{2}{3}y^{\frac{8}{2}}\right) \tag{3}$$

Here we require that solution for which large y presents a wave traveling to the right. This allows us to rewrite (3) in terms of a second function of Hankel H^2 [8].

$$\psi = \sqrt{y}H_{\frac{1}{3}}^{(2)}\left(\frac{2}{3}y^{\frac{8}{2}}\right) \tag{4}$$

$$\text{y} \gg 1 \Rightarrow \psi \sim \left(\frac{2}{\pi}\right)^{\frac{1}{2}}\ \left[\left(y^{\frac{1}{4}}\right)\left(\frac{2}{3}\right)^{\frac{1}{2}} \exp\left(-i\left[\frac{2}{3}y^{\frac{8}{2}} - \frac{5\pi}{12}\right)\right] \tag{5}$$

$$\text{y} \longrightarrow \infty \Rightarrow |\psi|^2 \sim \frac{A}{(W-C+FX)^{\frac{1}{2}}} = \frac{A'}{v'}$$

A, A': $constants$

v: Velocity of electrons.

$$\text{x} < 0\text{:}\ \ \psi = \frac{1}{W^{\frac{1}{4}}}\left[ae^{i\kappa x\sqrt{w}} + a'e^{-i\kappa x\sqrt{w}}\right] \tag{6}$$

Now we examine $H_{\frac{1}{3}}^{(2)}$ as it passes back through x = 0 from large x through the zero of y. We find no ambiguity here for ψ, since it is represented by a power series of integral powers of y. In order to proceed with the normal asymptotic expansion for $H_{\frac{1}{3}}^{(2)}\left(\frac{2}{3}y^{\frac{8}{2}}\right)$, over the valid range of $-2\pi < \arg\left(y^{\frac{8}{2}}\right) < \pi$, we assert that $y = -y = y'e^{-i\pi}$. The expansion about x = 0 is thus,

<u>X = + 0:</u>

$$\psi(0) = \left(\frac{C-W}{F}\right)^{\frac{1}{2}} e^{-0.5i\pi}(\kappa^2 F)^{\frac{1}{6}} H_{\frac{1}{3}}^{(2)}\left(e^{-\frac{3}{2}i\pi}\frac{2}{3}\kappa\sqrt{F}\left(\frac{C-W}{F}\right)^{\frac{3}{2}}\right)$$

$$\left(\frac{d\psi}{dx}\right)_0 = \frac{1}{2}\left(\frac{C-W}{F}\right)^{-\frac{1}{2}} e^{0.5i\pi}(\kappa^2 F)^{\frac{1}{6}} H_{\frac{1}{3}}^{(2)}\left(e^{-\frac{3}{2}i\pi}\frac{2}{3}\kappa\sqrt{F}\left(\frac{C-W}{F}\right)^{\frac{3}{2}}\right)$$

$$-\left(\frac{C-W}{F}\right)^{\frac{1}{2}}(\kappa^2 F)^{\frac{1}{6}}\kappa(C-W)^{\frac{1}{2}} H_{\frac{1}{3}}^{(2)\prime}\left(e^{-\frac{3}{2}i\pi}\frac{2}{3}\kappa\sqrt{F}\left(\frac{C-W}{F}\right)^{\frac{3}{2}}\right)$$

We can simplify the previous equation by omitting any common factor by absorbing it into the emission coefficient $|a|^2/|a'|^2$, which is the only quantity of interest physically. Thus we can write,

$$H_{\frac{1}{3}}^{(2)\prime}\left(e^{-\frac{3}{2}i\pi}Q\right) = e^{\frac{3}{2}i\pi}\frac{dH_{.033}^{(2)\prime}}{dQ}\left(e^{-\frac{3}{2}i\pi}Q\right)$$

$$Q = \tfrac{2}{3}\kappa\sqrt{F}\left(\tfrac{C-W}{F}\right)^{\frac{3}{2}}$$

With this the equations of continuity for ψ and dψ/dx can be reduced to,

$$a + a' = W^{\frac{1}{4}}\left(\tfrac{C-W}{F}\right)^{\frac{1}{2}} H_{\frac{1}{3}}^{(2)\prime}\left(e^{-\frac{3}{2}i\pi}Q\right) \tag{7}$$

$$-a + a' = \frac{i}{\kappa W^{\frac{1}{4}}}\left[\frac{1}{2}\left(\tfrac{C-W}{F}\right)^{\frac{1}{2}} H_{\frac{1}{3}}^{(2)}\left(e^{-\frac{3}{2}i\pi}Q\right) + \tfrac{C-W}{F}\kappa\sqrt{F}\,\tfrac{dH_{.033}^{(2)\prime}}{dQ}\left(e^{-\frac{3}{2}i\pi}Q\right)\right] \tag{8}$$

By definition of Hankel functions [8],

$$H_{\frac{1}{3}}^{(2)}\left(e^{-\frac{3}{2}i\pi}Q\right) = -\frac{1}{Sin\left(\frac{\pi}{3}\right)}\left\{I_{-0.33}(Q) + e^{\frac{1}{3}i\pi} I_{0.33}(Q)\right\} \tag{9}$$

Where $I_{\pm 0.33}(Q)$ is a real function and can be decomposed as,

$$\alpha + i\beta = \frac{I'_{-0.33}(Q) + e^{\frac{1}{3}i\pi} I'_{0.33}(Q)}{I_{-0.33}(Q) + e^{\frac{1}{3}i\pi} I_{0.33}(Q)}$$

With this, we can finally find a function, D(W), for the fraction of W electrons penetrating the boundary peak and emerging in the influence of an external field F. We do this by explicitly solving (7) and (8) using (9) in terms of $\alpha + i\beta$. After a bit of rearranging and referencing [8] we find,

$$D(W) = \frac{|a|^2 - |a'|^2}{|a|^2}$$

$$= \frac{4\beta \left(\frac{C-W}{F}\right)^{\frac{3}{2}} \sqrt{F}}{\left\{W^{\frac{1}{4}}\left(\frac{C-W}{F}\right)^{\frac{1}{2}} + \frac{C-W}{\sqrt{F}} \frac{\beta}{W^{\frac{1}{4}}}\right\}^2 + \frac{1}{\kappa^2 W^{\frac{1}{2}}}\left\{\frac{1}{2}\left(\frac{C-W}{F}\right)^{\frac{1}{2}} + \frac{C-W}{\sqrt{F}}\ \kappa\alpha\right\}^2}$$

To calculate $\alpha\ and\ \beta$,

$$\beta = \frac{\sqrt{3}}{2} \frac{I'_{0.33} I_{-0.33} - I'_{-0,33} I_{0.33}}{(I_{-0.33} + 0.5 I_{0.33})^2 + 0.75 I_{0.33}^2}$$

Upon reference [8], we see that the numerator is the Wronskian of the Bessel Equation of purely imaginary argument, thus we have exactly that,

$$I_{0.33} I'_{-0.33} - I_{-0,33} I'_{0.33} = -\frac{2Sin\left(\frac{\pi}{3}\right)}{\pi Q}$$

For the denominator we say that Q>>1 and use the asymptotic expansion to find,

$$\left| Sin\left(\frac{\pi}{3}\right) H_{\frac{1}{3}}^{(2)}\left(e^{-\frac{3}{2}i\pi} Q\right)\right|^2 \sim \frac{3}{4}\frac{2}{\pi Q} e^{2Q} => \quad \beta \sim e^{-2Q}$$

Through the same process of using asymptotic values and expansions we are able to find that$\alpha = 1$, finally,

$$D(W) = \frac{4\left(\frac{C-W}{F}\right)^{\frac{3}{2}} \sqrt{F}e^{-2Q}}{\left\{W^{\frac{1}{2}}\left(\frac{C-W}{F}\right)+\right\} + \frac{1}{\kappa^2 W^{\frac{1}{2}}}\left\{\frac{1}{2}\left(\frac{C-W}{F}\right)^{\frac{1}{2}} + \frac{C-W}{\sqrt{F}}\,\kappa\right\}^2} \qquad (10)$$

When examining the denominator we can see that the terms independent of κ are dominant and thus the second term in the denominator is ignored. Upon substitution of Q we find,

$$D(W) = \frac{4\{W(C-W)\}^{\frac{1}{2}}}{C} e^{-\frac{4\kappa(C-W)^{\frac{3}{2}}}{3F}} \qquad (11)$$

We are now in a position to calculate the electron emission from a cold metal, this is often referred to as Cold Field Emission (CFE). We begin by using the formula for the number of electrons N(W) incident on a surface of unit area per unit time, with a kinetic energy W that is normal to the surface. This has been calculated by Nordheim [9] using Sommerfeld's theory [10], which is a general theory of relativistic Keplerian motion applied to the quantum theory of spectra.

$$N(W) = \frac{4\pi mkT}{h^3} L\left(\frac{W-\mu}{kT}\right)$$

$$L(\beta) = \int_0^\infty \frac{dy}{e^{\beta+y}+1}$$

μ, the parameter of the electron distribution in the Fermi-Dirac statistics equivalent of the thermodynamic partial potential of an electron $\sim f(E) = \left\{1 + \left[\exp\frac{(E-E_f)}{k_bT}\right]\right\}^{-1}$. Thus the emission current is given generally by,

$$I = \frac{4\pi m\epsilon kT}{h^3}\int_0^\infty D(W)L\left(\frac{W-\mu}{kT}\right)dW \qquad (12)$$

$$\epsilon: electronic\ charge$$

For low temperatures the integrand of $L\left\{\frac{W-\mu}{kT}\right\}$ is sensible only when $\frac{W-\mu}{kT} + y < 0$ and is thus unity. In this temperature limit it is sufficient to approximate $kTL\left\{\frac{W-\mu}{kT}\right\}$ is $\mu - W$ for $W < \mu\ else\ zero$. In general, W and μ are much greater than kT, and $\mu \ll C$. Therefore we can use our derived approximate solution for D(W) (11) above in (12).

$$I = \frac{16\pi m\epsilon}{Ch^3}\int_0^\mu \{W(C-W)\}^{\frac{1}{2}}(\mu - W)e^{-\frac{4\kappa(C-W)^{\frac{3}{2}}}{3F}}dW$$

It can be seen via inspection that the integrand is very large for the largest value of W, thus the integral can be approximated sufficiently as,

$$I = \frac{\epsilon}{2\pi h}\frac{\mu^{\frac{1}{2}}}{(\chi+\mu)\chi^{\frac{1}{2}}}F^2 e^{-\frac{4\kappa\chi^{\frac{3}{2}}}{3F}} \qquad (13)$$

$$\chi = C - \mu$$

The χ value in (13) is the thermionic work function [11] that corresponds to a chosen metal's properties. (13) can be rearranged in terms of current density J, by dividing the current by the emitting surface area $\left(\frac{A}{cm^2}\right)$, and express the work function in terms of volts and F in terms for the field strength volts per distance(V/cm). Thus, the emission current density can be written as,

$$J = 6.2x10^{-6}\frac{\mu^{\frac{1}{2}}}{(\chi+\mu)\chi^{\frac{1}{2}}}F^2 e^{-\frac{6.8x10^7\chi^{\frac{3}{2}}}{F}} \qquad (14)$$

Experimental results found by Fowler and Nordheim [3] suggest that electron emission in an external field is satisfactorily accounted for by (14).

Further rearranging of (14) into a form more readily used and slightly updated, based on work by R.G. Forbes[12], allows us to make some useful simplifications.

$$J = a\chi^{-1}F^{2}P_{F}\exp\left(-\frac{b\chi^{\frac{3}{2}}}{F}\right) \qquad (15)$$

$$P_{F} = \frac{4\chi^{\frac{1}{2}}\mu^{\frac{1}{2}}}{\chi+\mu}$$

$$a \sim 1.541434x10^{-6}AeV\;V^{-2}$$

$$b \sim 6.830890\;\; eV^{-\frac{3}{2}}\; V\; nm^{-1}$$

P_F is commonly known as the tunneling prefactor, and is usually of order unity and often ignored in the cold field emission theory referenced here.

Before we proceed, it would be useful to consolidate all of the assumptions made in this derivation for reference later in this text.

Assumptions:

- The temperature of the emitting metal surface is taken to be 0K, such that no electrons with energies above the fermi energy exist in the metal, and that the fermi level will be the top most filled level with electrons. Its electronic charge distribution in the metal given by the Fermi-Dirac statistics.

- Electron-Ion and Electron-Electron interactions are neglected. Known as the free electron approximation
- The emitting surface is taken to be rather smooth, such that irregularities are small compared to the width of the potential barrier (*i.e.* the size of the gap). Quantum Mechanical Tunneling [6,7] across the barrier occurs only if the uncertainty in the position, Δx, of the electron is of order the barrier width $i.e.\ x = \frac{\chi}{Ee}$
- The potential barrier near the surface in the vacuum region consists of a potential due to the applied electric field, known as an image potential. This potential exerts an image force by the Coulomb attraction towards the surface of an electron outside, due to the induced charge inside of the metal.

1.3) Fowler-Nordheim Plot

As shown in the previous section, the Fowler-Nordheim equation (15) determines the total number of electrons that tunnel through the potential barrier at the surface per unit area, also known as the emission current density. In order to use this analytical function experimentally, we must rearrange the terms slightly. Much like how we put our emission current in terms of current density, we will return to our original convention of current rather than current density, and we will now change our electric field strength coefficient to something that is measureable.

$$F = \beta V$$

$$I = JA$$

Where A is the emitting surface area in cm^2, β is the field enhancement factor in cm^{-1}(rather the ratio of the field at the surface to the anode-cathode voltage) and V is the anode-cathode voltage. The field enhancement factor is determined by the geometry of the emitter. Substituting these into (15) we find,

$$I = a\chi^{-1}\beta^2 V^2 P_F \exp\left(-\frac{b\chi^{\frac{3}{2}}}{\beta V}\right) \tag{15.5}$$

If we take the log of both sides and slightly rearrange some terms,

$$\log\left(\frac{I}{V^2}\right) = -\frac{(2.9669x10^7)\chi^{\frac{3}{2}}}{\beta V} + \log\left(a\frac{\beta^2}{\chi}\right)$$

A curve can be obtained by plotting $\log\left(\frac{I}{V^2}\right)$ versus $\frac{10000}{V}$ which in most cases yields a straight line, and is known as a Fowler-Nordheim (FN) plot. Taking the slope of this line gives,

$$m = -\frac{2.9669x10^3\chi^{\frac{1}{2}}}{\beta} \tag{16}$$

What is immediately interesting about this result is that our slope is only dependent on the known value of our work function (which is a determined factor for materials in NIST database), and the enhancement factor. This means that this enhancement value can be calculated experimentally.

1.3.1) Physical Meaning of Enhancement Factor

When discussing cold field emission theory [25] it is assumed that all electrons escape by a wave function based mechanical tunneling through an electric field lowered energy barrier, via states near in energy to the fermi energy level. For electrons, this is described by the Schrödinger equation, and has been derived explicitly in Chapter 1.1-1.2.

Consider now an electron traveling in a wave state k towards the mechanical barrier (potential barrier) at the emitter surface, then the probability that the electron will escape is D_k. Each wave state k has a small contribution from the incident current density, ζ_k, approaching the barrier from the inside with a contribution of $\zeta_k D_k$ to the emission current density,

$$J = \Sigma_k(\zeta_k D_k). \tag{17}$$

When comparing equation (17) to the emission current equation in the (15.5), it can be seen that as β increases, the emission current increases. An increase in current emission thus means an increase in the probability that an electron will tunnel through the mechanical (potential) barrier. Experimentally this increase in enhancement factor, and thus tunneling probability will be evaluated in the following chapters.

1.4) Existing Breakdown Geometry Data

In the early 50’s and 60’s, lots of experimental work was carried out on high voltage breakdown [26-32], generally centering on simple electrode geometry; point-plane, sphere-sphere. In an experimental paper by M. Okawa [13], the principles derived in the above section were put into practice experimentally to great effect. It was shown how the enhancement factor can be calculated from FN plots and plotted for a very large array of geometries that had not been tested previously, Figure-(3). Based on the theory outlined in the previous section, the FN plots (Figure-(4)) yield a rather straight line that can be used to determine the enhancement factor (Figure-5, 6). Figure 5,6 show a comprehensive trend in enhancement factor versus gap size for many different geometries. For simple geometries like sphere-sphere, and rod-plane a straight forward trend of increase in gap size yields an increase in enhancement factor on average, till a threshold gap distance is met and the enhancement factor plateaus. Where as in the more complex geometries, ring-ring and cylinder-plane, it is shown that enhancement factor follows a much more complex trend, with sharp increases and decreases as gap size changes.

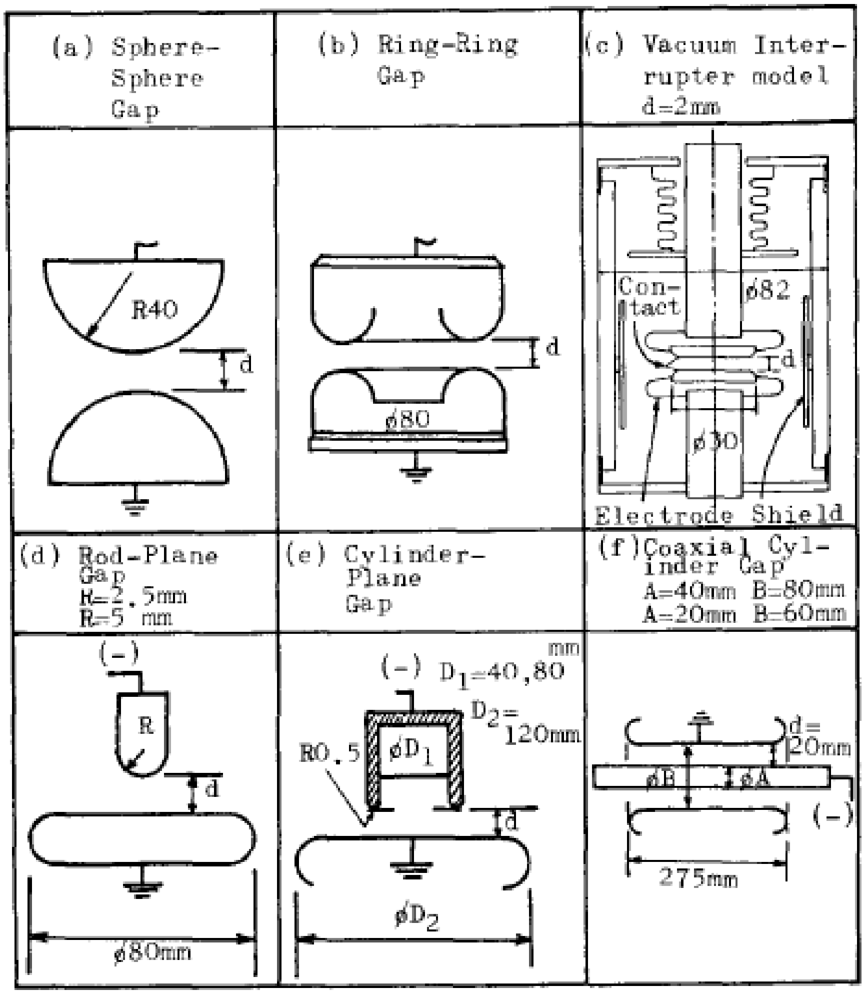

Figure 3: Experimental Geometries presented by M.Okawa [13]

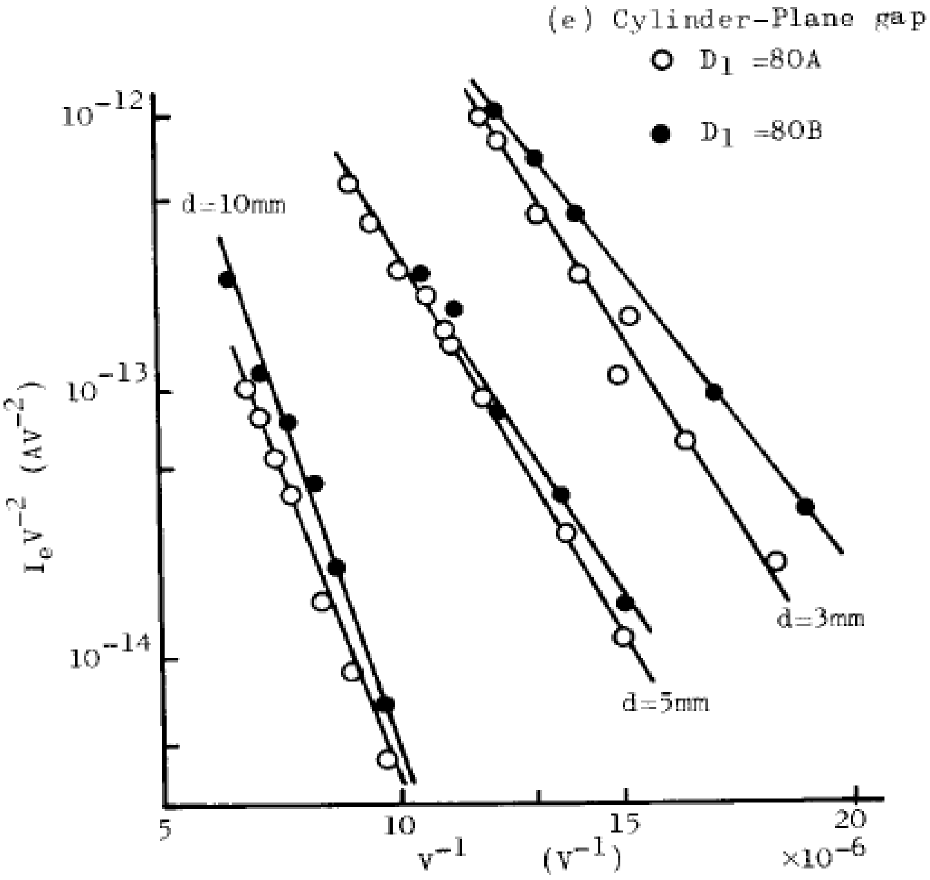

Figure 4: FN Plots based on experimental results for Cylinder-Plane gap.

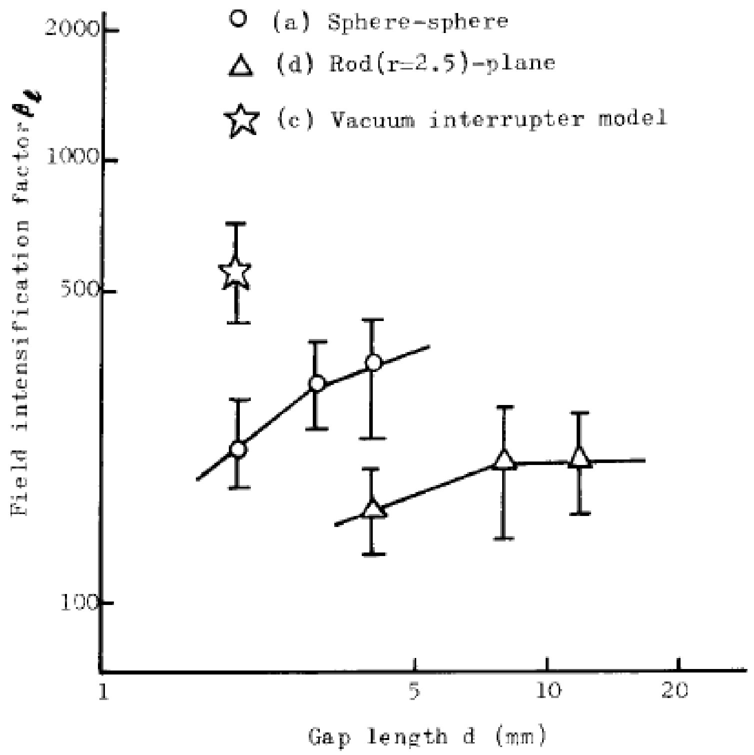

Figure 5: Enhancement factor versus separation gap length for (a) Sphere-Sphere and (d) Rod-Plane.

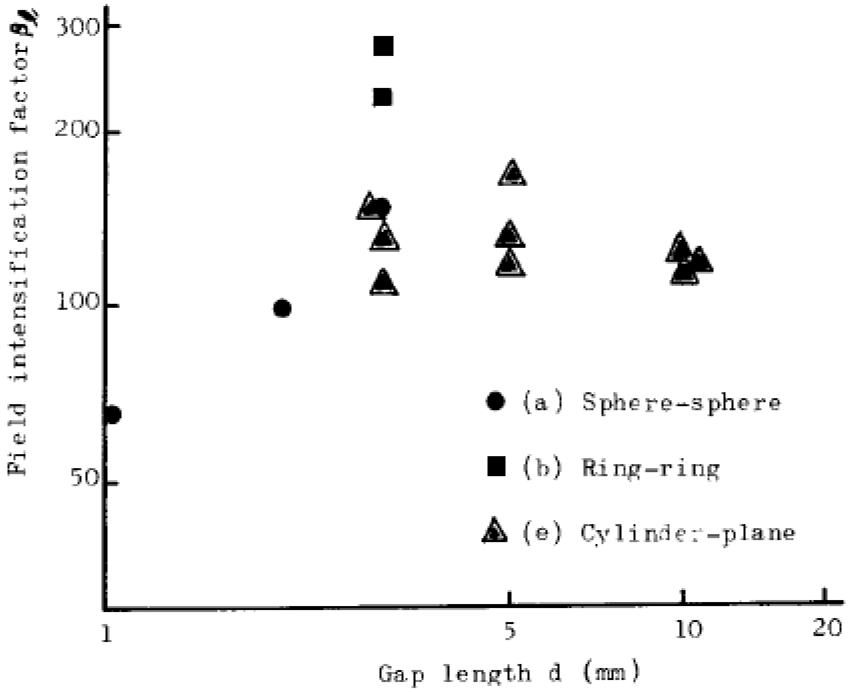

Figure 6: Enhancement factors versus separation gap length for (a)Sphere-Sphere, (b) Ring-Ring, and (e) Cylinder-plane.

The pertinent results found by M.Okawa are as follows; the enhancement factor β m presents different values for the same gap length and for gap lengths that differ, as well as for different geometries. This means that breakdown initiation and thus current emission and probability of tunneling is influenced by gap size. Furthermore, the fact that the enhancement factor changes even in the same geometry and gap size would indicate that the surface area of the breakdown plays a role in the value of the enhancement factor. It was further shown upon inspection of the electrode surface after breakdown, that all breakdown traces are concentrated in a region with >90% of some maximum field strength, $E = \beta\left(\frac{V}{Gapsize}\right)$. This region is known as an effective surface area, and is determined experimentally through direct measurement. This allows one to take into account multiple formations of emission current, where previous work only considers a single breakdown point due to the geometry tested. These results will be referenced later in the text.

Note, the graphs here are presented in β_l which is determined by,

$$\beta_l = NS_{eff}^{x}$$

where N is a form factor depending on the metal used, x is the average slope of field strength vs. gap length for each geometry. S_{eff} is the effective surface area of breakdown, which is determined via imaging of the electrode surface.

1.5) Liner Loads on the Sandia Z-Machine

High gain inertial fusion has eluded researchers for many years, and has lead to a robust amount of high energy density research and the development of many different approaches to fusion. One such approach, in the Z-pinch community, is the compression of a magnetized solid liner filled with DT fuel combined with modular linear transformer driver pulsed power devices. Such an approach is more commonly known as magnetized liner inertial fusion (MagLIF) and was first described by Slutz, *et al.*[14]. This is currently being studied at the Sandia Z-Machine. The approach makes use of a hollow aluminum (or beryllium) cylindrical liner (h~10mm,D~6mm, W~300μm) which contains the DT fuel. External magnetic field coils that produce fields up to B_{axial}~30T are applied prior to the main current pulse in order to reduce heat loss via electron-alpha particle transport, and help stabilize in inner liner wall Magneto-Rayleigh Taylor instabilities (inherent in the hydrostatic MHD calculation for the z-pinch[]). Once the external magnetic field has penetrated the liner, radial compression is initiated via a current pulse (20MA,100ns).

Of specific importance to this work is the way in which the liner is mounted to the cathode power feed in the Z-machine. Typically, the liner is fixed to the upper anode and then this entire unit is inserted into the cathode which is fixed to the power feed. Once this step is completed a small azimuthal vacuum gap ($\sim 25\mu m$) between the liner and the cathode remains, as seen in Figure-7. The existence of this gap will be referenced and further explored in later chapters of this text.

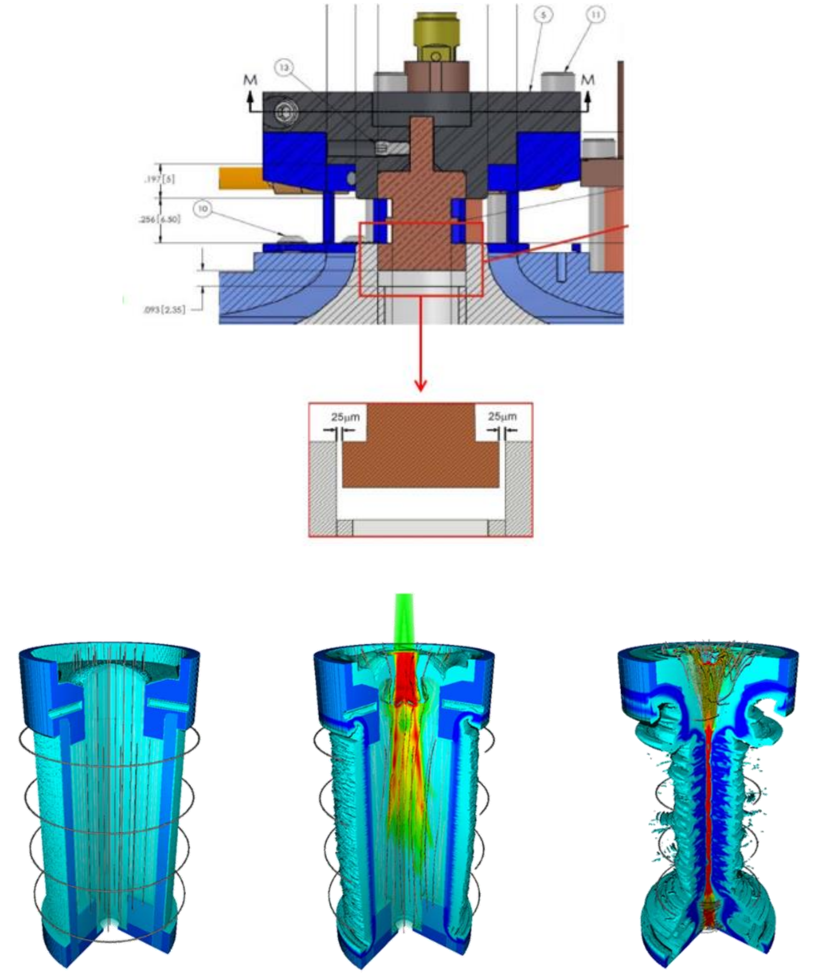

External Axial B-field
Liner driven by >20MA

Fuel laser heated
to improve yield

Liner implosion compresses
fuel, as well as axial B-field to
improve confinement

S. A. Slutz *et al*, *Physics of Plasmas*, **17**, p056303. (2010)

Figure 7: Solidworks drawing of the azimuthal gap in the Z-machine and MHD simulation of MagLIF stages.

At this point it is now useful to outline a semi-analytical model of a few specific processes in MagLIF based entirely on calculations performed by R.D McBride [15]. The calculations below are based on Figure-8, where the system has been divided into three distinct regions, vacuum region, liner region, and fuel region. As described in the MagLIF process above, a uniformly distributed axial magnetic field is in each region before the axial current is turned on. The radius of each region is labeled according to region, with r being the total radius, r_L being the radius of the liner, and r_g being the radius of the fuel.

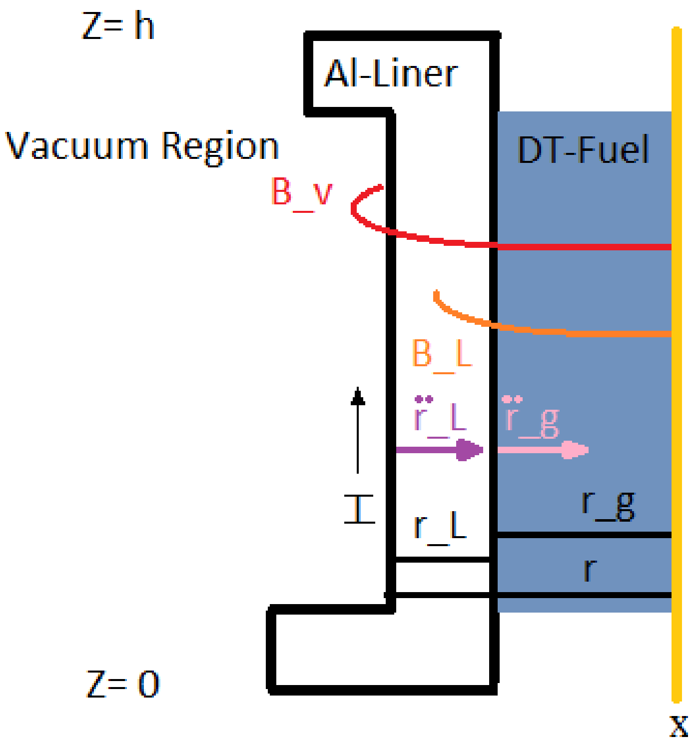

Figure 8: 2-D Slice of the Al liner of the MagLIF experiment. Where x is the center of the liner and the axis of compression

The implosion of the liner and the fuel are driven by the pressure of the azimuthal magnetic field, which is supplied by the pulsed power driver of the Z-machine. Based on the cylindrical geometry the field generated in the vacuum regions is,

$$B_v = \frac{\mu_0 I_{liner}}{2\pi r} \qquad (1)$$

Here we assume that, like in our figure-8, that the azimuthal B-field is partially diffused into the liner wall, and can be described as such,

$$B_L = \frac{\mu_0 I_{liner}}{2\pi r_L}\left(\frac{r-r_g}{r_L-r_g}\right)^{\beta} \qquad (2)$$

Where β is a found quantity based on the skin depth ,δ_{skin}, of the material and is as follows.

$$\beta = \max\left\{1, \left|\frac{\ln\left(\frac{1}{e}\right)}{\ln\left(\frac{\delta_{I0}-\delta_{skin}}{\delta_{I0}}\right)}\right|\right\} \qquad (3)$$

$$\delta_{skin} = \sqrt{\frac{4\rho_e\tau_r}{\pi\mu_0}}$$

$\rho_e: \mathit{Initial\ electrical\ resistivity\ of\ liner\ mater}$

$\tau_r: \mathit{rise\ time\ of\ the\ current\ driving\ the\ azimuthal\ magnetic\ field}$

$\mu_0: \mathit{is\ the\ typical\ permitivity\ of\ free\ space}$

Some useful values have been provided in the table below.

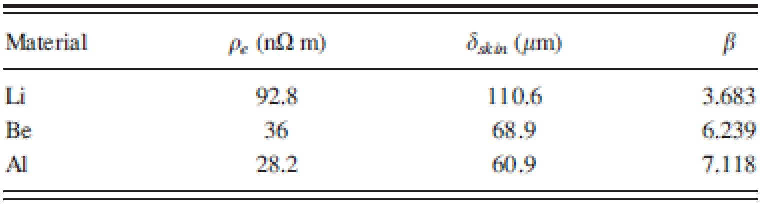

Material	ρ_e (nΩ m)	δ_{skin} (μm)	β
Li	92.8	110.6	3.683
Be	36	68.9	6.239
Al	28.2	60.9	7.118

Figure 9: Values calculated with τ_r= 130 ns

With this we are now able to consider liner dynamics and compression. To account for the compressibility of the liner, the liner is divided up into $N_{ls} \geq 20$ concentric thin liner shells. We can write an equation of motion for each liner interface, as well as for the liner-fuel interface (which is an internal interface) and the liner-vacuum interface (which is known as an external interface). The internal interfaces are assigned a mass, $m_{ls} = m_l/N_{ls}$. Where m_l is the total liner mass. Each external interface has a mass of $m_{ls}/2$. In total there are $N_{li} = N_{ls} + 1$ liner interfaces. The radial position of each liner interface,r_{li}, are distributed over $\left[r_g = r_{l,i=1}, r_l = r_{l,i=Nli}\right]$ with an initial radial interface position $i + 1$, denoted by

$$r_{l,i+1}(t_0) = \sqrt{r_{l,i}^2(t_0) + \frac{m_{ls}}{\pi h \rho_{l0}}}\ (i = 1, \dots N_{li} - 2). \qquad (4)$$

$$\rho_{l0}: intial\ mass\ density\ of\ liner\ material$$

The center of mass radial position of the liner shell s is given by,

$$r_{l,i+1}(t) = \sqrt{\frac{[r_{l,i=s}^2(t) + r_{l,i=s+1}^2(t)]}{2}}\quad (s = 1, \dots N_{li}). \quad (5)$$

Here we have N_{li} interfaces, and thus N_{li} equations of motion. Thus, the equation of motion for the internal interface of the liner is given by

$$\ddot{r}_{l,i} = \frac{p_{l,s=i-1} - p_{l,s=i}}{m_{l,s}}\ 2\pi r_{l,i} h\ (i = 1, \dots N_{li} - 1). \qquad (6)$$

Here $p_{l,s}$ is the effective pressure in the liner shell, s. The effective pressure is made up of the material pressure,$p_{ml,s}$, azimuthal magnetic field pressure, $p_{Bazimuth\ l,s}$, axial magnetic fieldpressure, $p_{Baxial,l,s}$, and a pseudo-pressure from the artificial viscosity, $q_{l,s}$. Similarly the equation of motion for the fuel interface is

$$\ddot{r}_g = \frac{p_g + p_{Baxial,g} - p_{l,s=1}}{\frac{m_{l,s}}{2}}\ 2\pi r_g h \qquad (7)$$

With,p_g, being the gas pressure in the fuel region, and $p_{Baxial,g}$ an average axial magnetic field pressure in the fuel region, the equation of motions for the liner-vacuum interface region is

$$\ddot{r}_l = \frac{p_{l,s=N_{l,s}} - p_{Bazimuth,l,v} - p_{Baverage_{axial},v}}{\frac{m_{l,s}}{2}} \, 2\pi r_l h \qquad (8)$$

Here ,$p_{Bazimuth,l,v}$, is the pressure of the azimuthal magnetic field at the liner-vacuum interface $(r = r_l)$, $p_{Baverage_{axial,v}}$, is the pressure due to the average axial magnetic field in the vacuum region. Where the magnetic pressure (in axial and azimuth) in all regions is just,

$$p_B(r) = \frac{B^2(r)}{2\mu_0} \qquad (9)$$

The fuel region is assumed to be isobaric $(\nabla p = 0)$, and for MagLIF the gas pressure tends to dominate the magnetic field pressure in the fuel region, thus the magnetic field in the fuel is the average axial field

$$B_{average_{axial,g}} = \frac{\phi_{axial,g}}{\pi r_g^2} \qquad (10)$$

$\phi_{axial,g}$: is the total axial magnetic flux in the fuel.

In the liner region, it is assumed that $B_{axial,l}(r)/\rho_l(r) = constant$, so for the associated axial magnetic pressure in the liner we use,

$$B_{axial,l,s} = B_{average_{axial,l}} \frac{\rho_{l,s}}{\rho_{average,l}} \qquad (11)$$

$$B_{average_{axial}} = \frac{\phi_{axial,l}}{\pi(r_l^2 - r_g^2)} \qquad (12)$$

$\phi_{axial,l}: Total\ axial\ magnetic\ flux\ in\ liner\ region$

$$\rho_{average,l}: average\ mass\ density\ in\ the\ liner\ region.$$

$$\rho_{l,s}: mass\ density\ of\ the\ shell\ s$$

$$\rho_{average,l} = \frac{m_l}{\pi(r_l^2 - r_g^2)h} \qquad (13)$$

$$\rho_{l,s} = \frac{m_{ls}}{V_{l,s}} \qquad (14)$$

$$V_{l,s} = \pi\left(r_{l,i=s+1}^2 - r_{l,i=s}^2\right)h \qquad (15)$$

$$V_{l,s}: volume\ of\ the\ shell, s$$

For the magnetic pressure in the vacuum region due to the axial magnetic field, we use the average axial magnetic field.

$$B_{axial,v} = \frac{\phi_{axial,v}}{\pi(r_{rc}^2 - r_l^2)} \qquad (16)$$

$$\phi_{axial,v}: total\ axial\ magnetic\ flux\ in\ the\ vacuum\ region.$$

For the magnetic pressure in the liner and vacuum, due to the azimuthal magnetic field, we use,

$$B_{azimuth,lv} = B_{azimuth,l}(r_l) = B_{azimuth,v}(r_l) = \frac{\mu_0 I_l}{2\pi r_l} \qquad (17)$$

which leads to,

$$p_{azimuth,lv} = \frac{B_{azimuth,lv}^2}{2\mu_0} = \frac{\mu_0 I_l^2}{8\pi^2 r_l^2}\ . \qquad (18)$$

Thus, we have a fully defined 1-D pseudo-analytical description of the equations of motion corresponding to our Figure-8. This model is referenced closely in Chapter 4, and will aid in proving the relevance to MagLIF that this text will outline in the following chapters, as was stated in Chapter 1.

However, it is important to restate here that this is a solely 1-D calculation, and not directly relevant to the 3-D discussion that much of the data presented here covers. The way this will be resolved is that the inherent assumption in these calculations of uniform current distribution will be removed and the calculation in Chapter 4 will be made with an asymmetric non-uniform current distribution in a mirrored 1-D analogy to what is described above.

Chapter 2: Coaxial Gap Breakdown Machine

An experimental system has been developed at the University of California San Diego to study the mechanisms and influences of coaxial geometry vacuum gaps. The basic design of the coaxial gap breakdown experiment was first developed by Dr. Bott-Suzuki, and a student, Cole Meisenhelder, from the National Undergraduate Fellowship (NUF) summer program in 2014. Initial results showed interesting optical images with azimuthal breakdown distribution, but with a few inconsistencies and several new problems to investigate with many parameters with which to work. Problems such as: what are the mechanisms responsible for the breakdown of a coaxial gap? Are breakdowns random about the azimuth? Can breakdown position be known without line of sight imaging? What effects does azimuthal distribution of breakdown have later in time on the early time evolution of the magnetic field, and how does it scale for pulsed power liners used on mega ampere (MA) machines, such as COBRA at Cornell University? The project has since been upgraded to answer such questions, and the full design and diagnostics will be described in detail in this chapter.

2.1) Electrode Design

The Coaxial Gap Breakdown experiment consists of two aluminum electrodes: a hollow cylinder (R_{outer} = 6.09 mm-anode), with an inserted solid cylinder, with radii from $25\mu m - 1.5mm$, and all 5cm in length. Both are attached to 3-D electric translational mounts so as to ensure the electrodes are parallel to one another (Figure 10) before and after vacuum pressure (<$10^5 Torr$) is achieved.

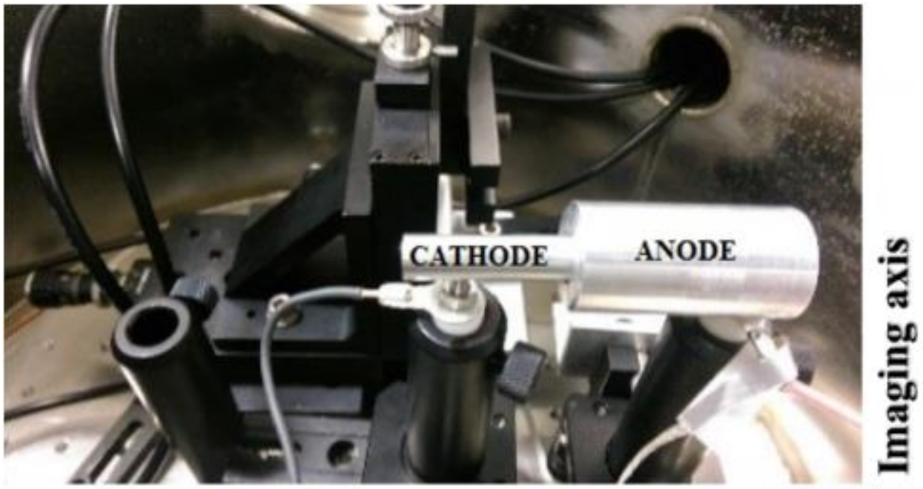

Figure 10: Aluminum electrodes attached to 3-D electronic translational mounts.

The electrodes are machined in-house. Each electrode has a surface finish with features of order ~5-10μm as shown in Scanning Electron Microscope (SEM) surface profile images (Figure -11a,b), taken at the Nano3 Cleanroom Facility on the UC San Diego campus. The surface finish here indicates a potential for multiple field enhancement points, as is required in the cold field approximation. It is important to note that while the electrodes used for this work are cleaned following machining, they are not further polished or treated.

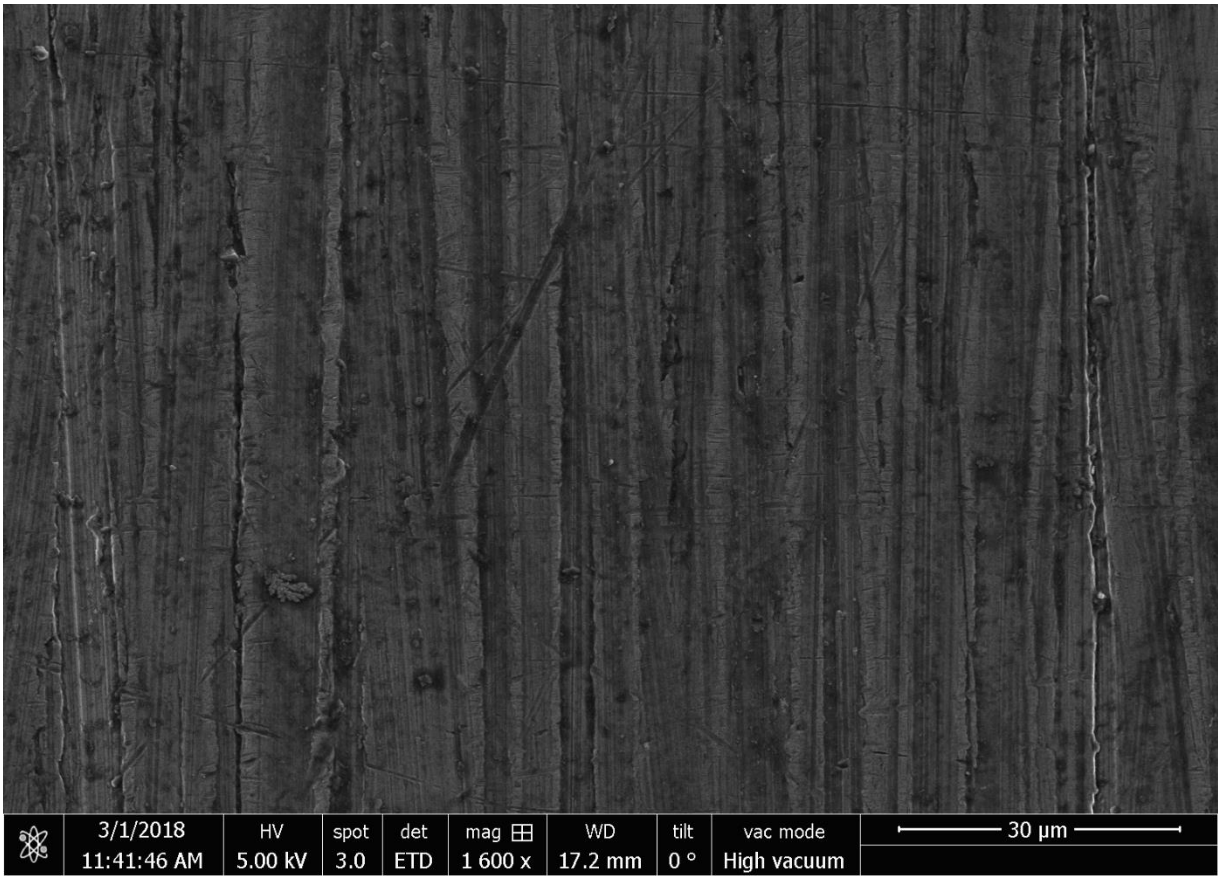

Figure 11 (a): $330\mu m$ gap electrode SEM image

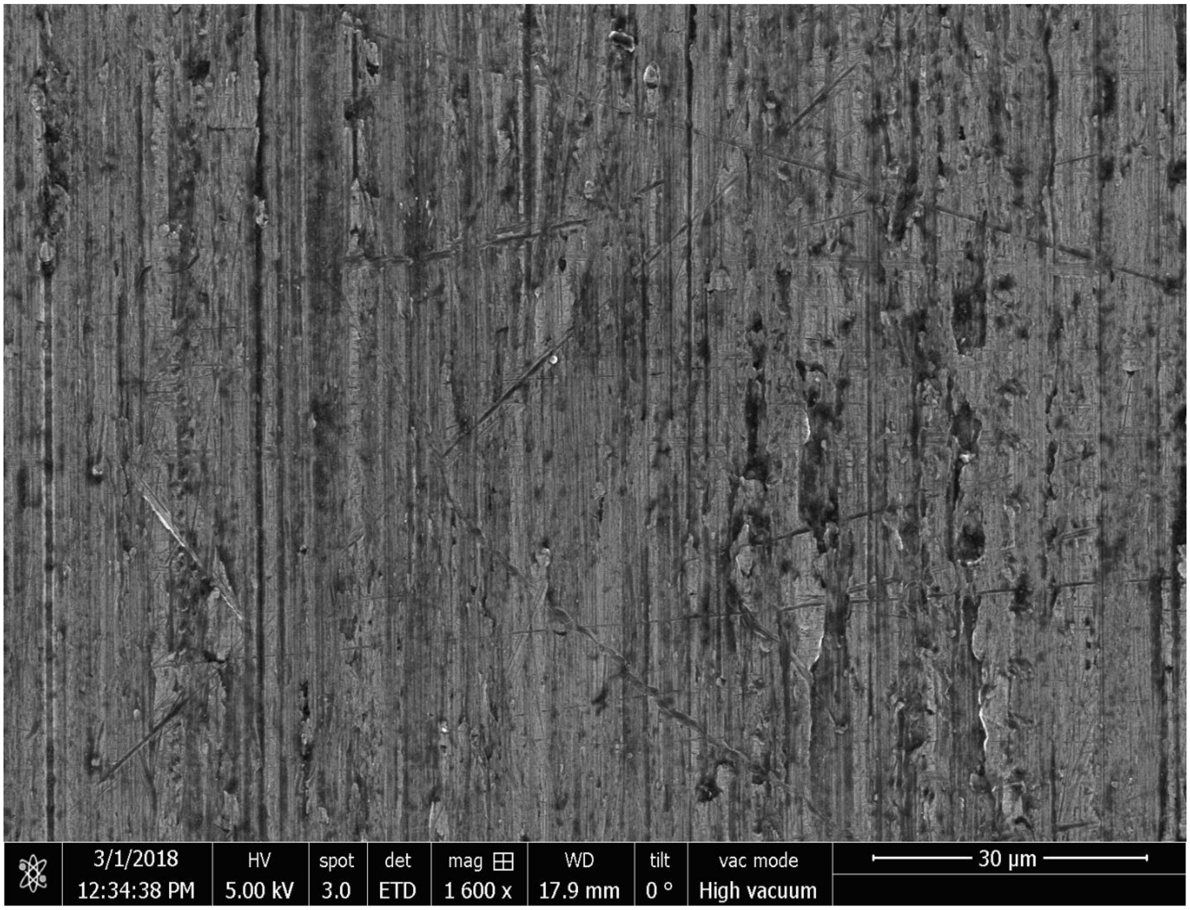

Figure 11 (b): $1150\mu m$ gap electrode SEM image.

2.2) Circuit Design

The implemented experimental circuit follows the simple charging circuit design shown in Figure-12. Standard resulting Current (240A, 150ns) and Voltage (25kV) profiles are shown in Figure-13. The circuit is triggered via custom made trigatron switch [16] Figure-14.

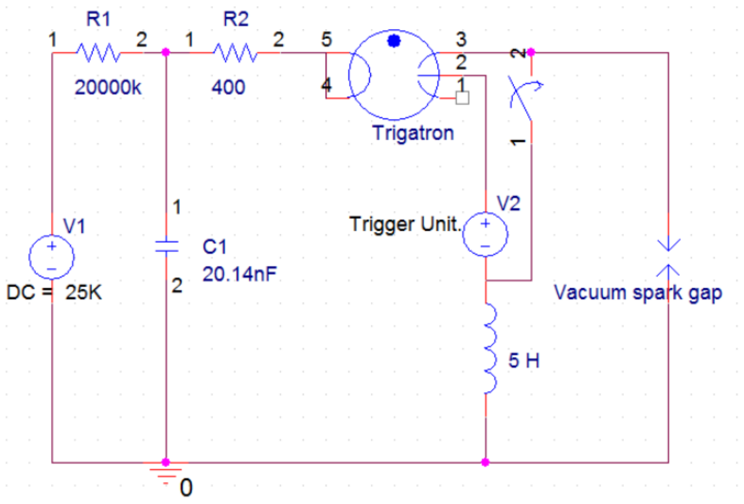

Figure 12: Pulsed power charging circuit diagram.

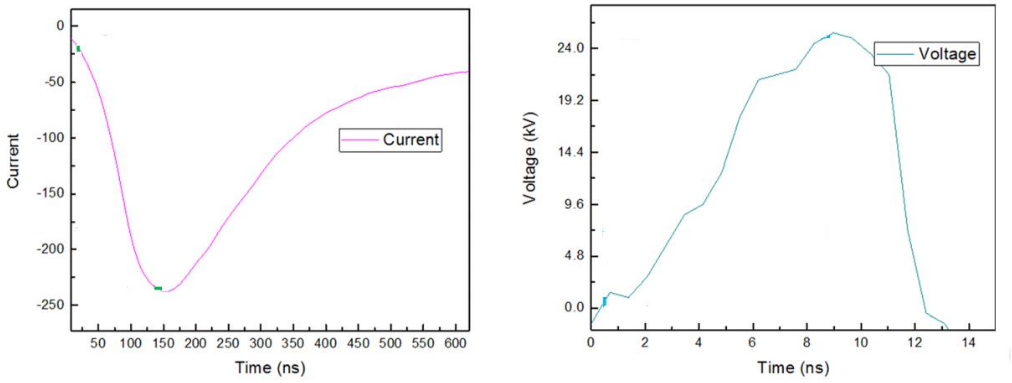

Figure 13: Standard operating current and voltage pulses

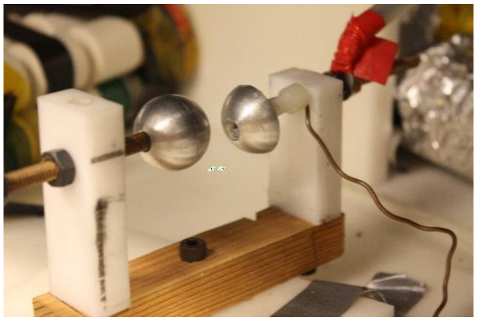

Figure 14: Trigatron design

2.2) Rep-Rate Upgrade

In a push to generate a statistically relevant amount of data, the experimental machine was upgraded to a repetition rated machine that fires and collects data at 0.076 Hz (*i.e*. 1 shot every 13 seconds). This was achieved by linking together all components required to trigger and collect data in the system and consolidating them into one tower, or command center, as seen in Figure-14. The tower consists of: Two oscilloscopes, high voltage power supply, high voltage signal generator, two relay switches, two DG535 signal generators, and two linked computers (XP legacy & Windows 7 Machine). The command center is fully automated via a custom Java program that utilizes the Robot Class [17] to integrate and control programs such as: IEEE Signal Express, a Custom HP oscilloscope data collection software, XP custom printer port triggering program. The automation process is described by the flow chart in Figure-15.

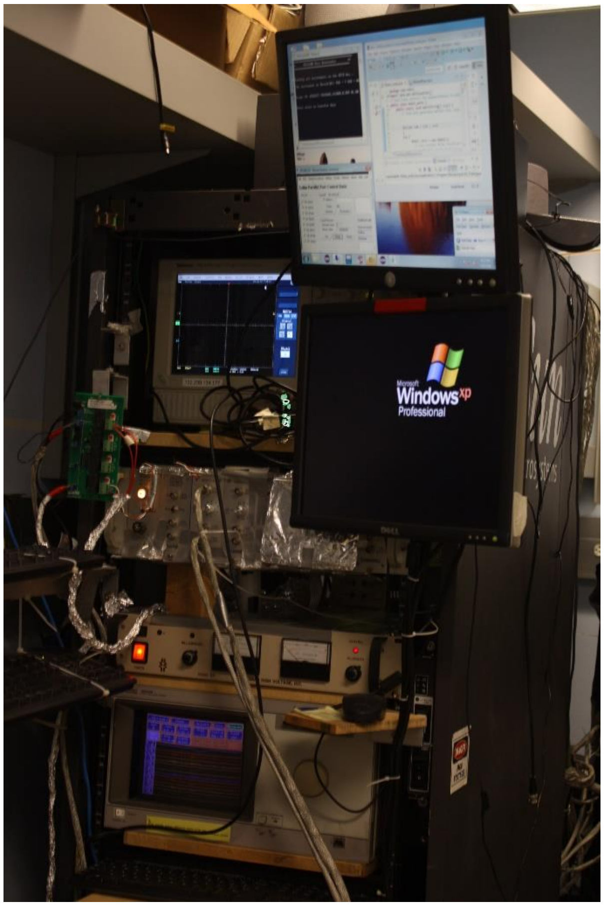

Figure 14: command center- Master control tower for coaxial gap break down rep-rated machine.

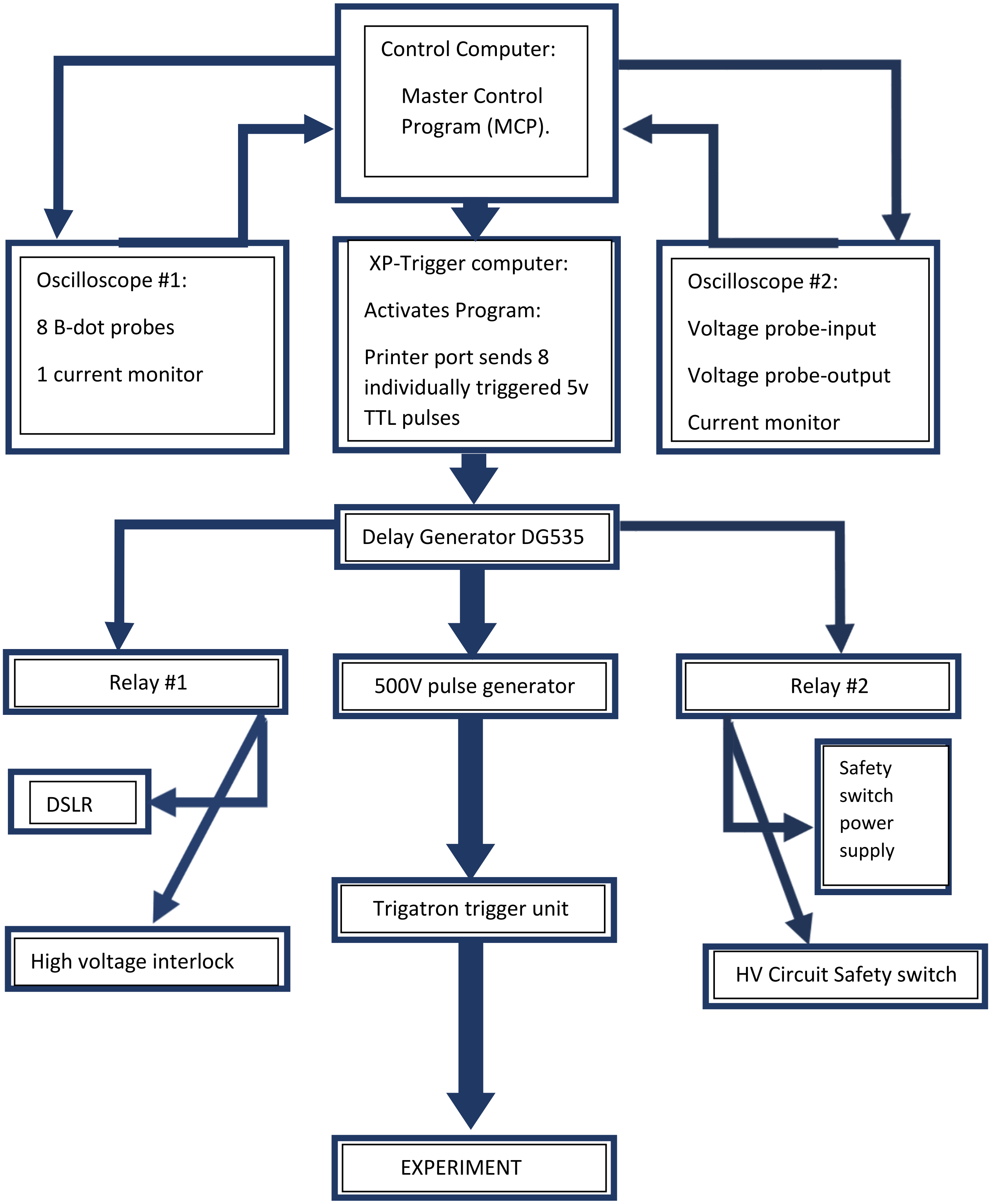

Figure 15: Automation Flow Chart for a single iteration, arrows denote direction of communication.

2.3) Diagnostics

The vacuum gap was monitored by several diagnostics. Current was measurement *via* Pearson coil (model 6585, 1.5 ns rise time), and a pair of high voltage probes (Pintek-HVP-39pro) monitored the HV at both the high voltage and ground side of the electrodes. Time-integrated optical images are taken along the electrode common axis on every shot, and the current density in monitored by an array of magnetic (dB/dt) probes as described in the next sections.

2.3.1) Magnetic Field Probes

Magnetic field probes are made using semi-rigid coaxial cable (rg405/u). The cable is cut to the dimensions specified in Figure 16. The inner wire of the coaxial cable is wrapped in a kapton layer to ensure that each loop does not touch and prevent any breakdown between them. The area of each loop is made in the same fashion by wrapping the loops around an uncut semi-rigid coaxial cable of diameter 3.56 mm. The number of loops on each probe is determined by the operating conditions of the experiment. In this case, it was determined that for the Coaxial Gap Breakdown machine (220 A, 25 kV, 130 ns) a three loop probe at a radial distance of 2-4mm was the optimal setup. Furthermore, it is important that the connection of the loop to the outer shielding of the coaxial cable is sound as this reduces noise of the measured magnetic field signal.

Probes are calibrated through direct area measurement of the coils on each probe, with final sensitivity of each probe determined by a short circuit on the CGB machine. Starting with a known short circuit current pulse and known location of the center of B-dot probes with respect to the center of the electrode setup before the shot, we can calculate the expected magnetic field signals for each probe. Comparing the expected signals to those of the measured signals (Figure 17) we find that generally the measured signals match closely with both the current trace and the expected signals. Upon closer inspection, we find that the percent difference away from expected values of each probe is less than five percent. These percent difference values are then added to the calculated calibration factor of each probe to ensure a complete and accurate calibration. This small percent difference indicates that the direct area measurement is rough yet sufficient alone to calibrate accurate B-dot probes.

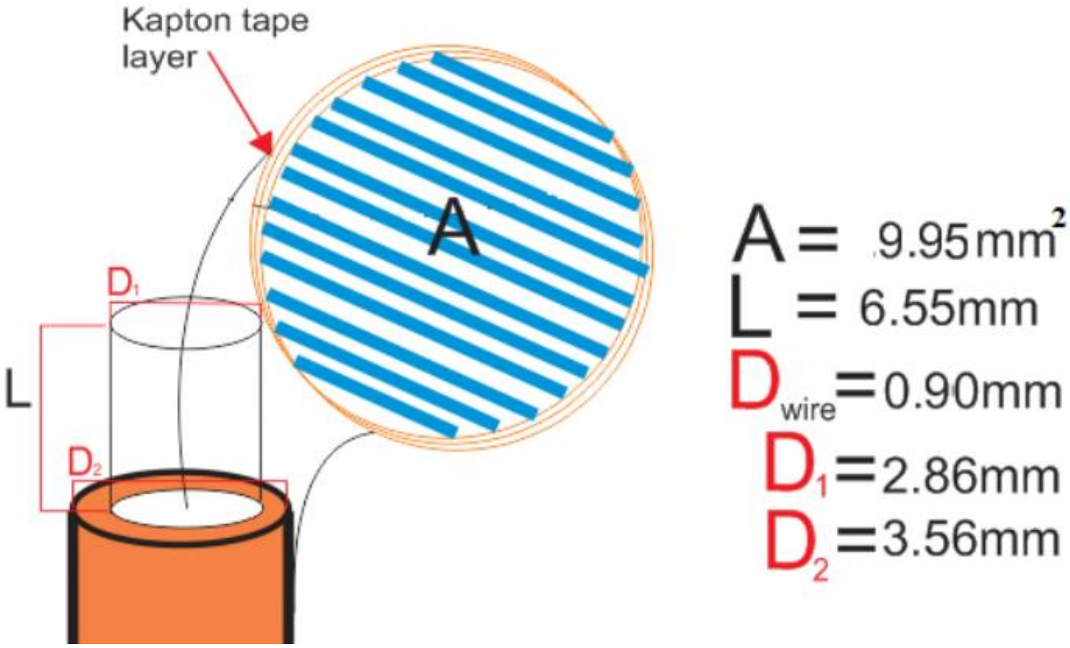

Figure 16: Magnetic Field probe dimensions.

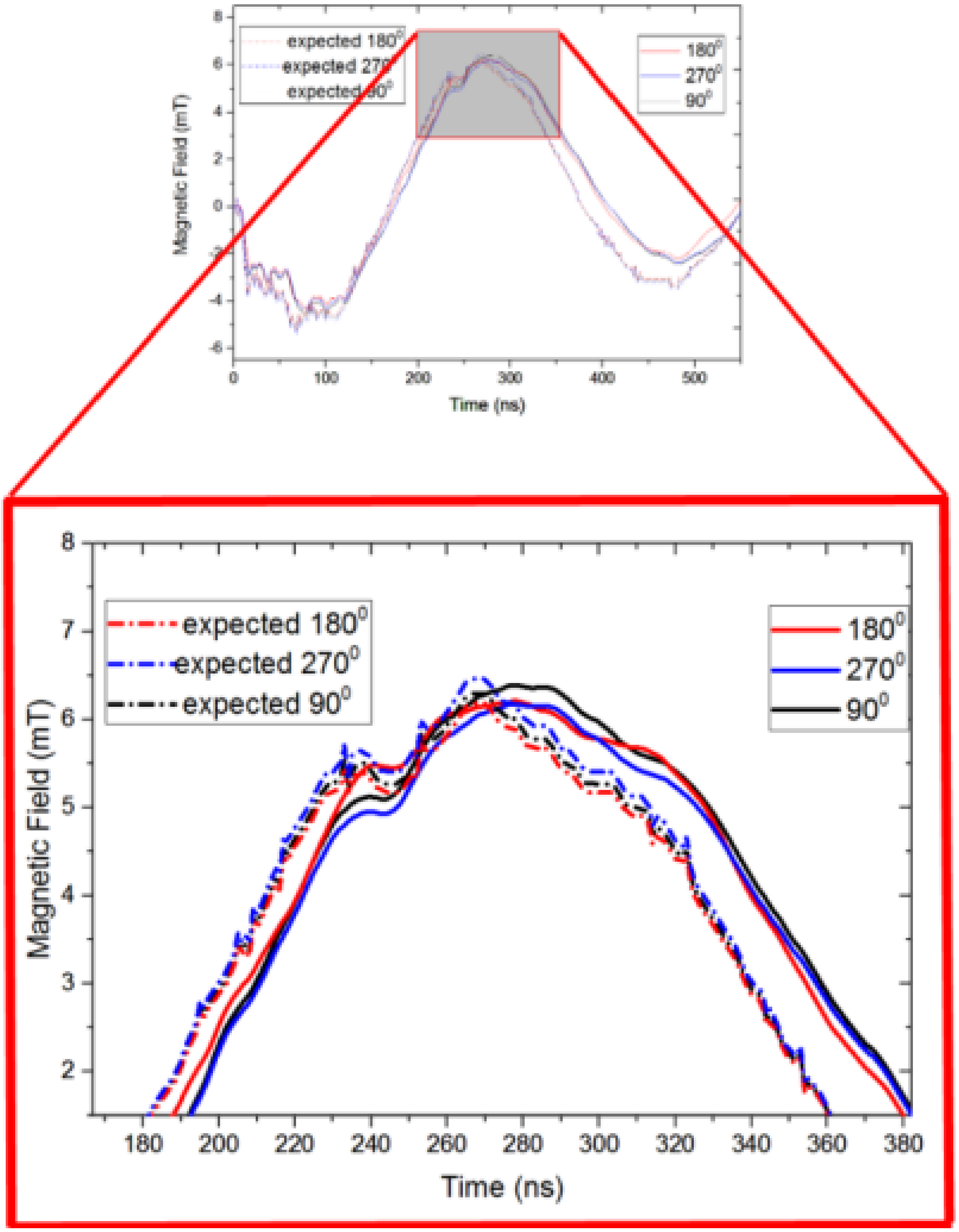

Figure 17: typical measured short circuit current and magnetic field calibration signals.

2.3.2) Triangulation Technique

Through experimentation on the CGB, a comprehensive method to determine the exact location of breakdown in a coaxial gap has been developed using an array of magnetic field (B-dot) probes. To do this, we first calculate the magnetic field at peak current, by using

$$V_{gen} = -N\frac{d\phi}{dt} \rightarrow B = \frac{1}{AN}\int V dt, \tag{19}$$

where V is the measured voltage generated by the magnetic field flux through a loop of area A, and N is the number of loops. Then, we take the calculated magnetic field for each B-dot probe, and use it to calculate the distance away (R) the breakdown occurred from the probe by use of Equation (20) at peak current (I).

$$\oint_C \mathbf{B} \cdot d\mathbf{L} = I_{enc} \rightarrow R = \frac{\mu I}{2\pi B} \tag{20}$$

By generating three circles with origins located in the center of the corresponding B-dot loop of each probe, and radii corresponding to the different distance away from breakdown (R) for each probe, the intersection of these three circles can be observed and thus triangulate the absolute position at which the breakdown has occurred. When the triangulation data are overlaid on corresponding time integrated optical images, it is observed that the triangulation method determines the exact position where the breakdown has occurred. The accuracy of the 3 probe triangulation method means that the technique can be used to determine the exact position of a single breakdown in a coaxial gap even when time integrated axial optical emission imaging is not possible.

In order to maximize the effective mapping area of a coaxial gap, a minimum of three B-dot probes placed at 90◦ intervals around the circumference of the anode (Figure 18) are needed.

The distance away from the anode each probe is placed is determined by the experiment and the sensitivity of the probes. Due to the location of the B-dot probes with respect to the vacuum gap, the probes do not read magnetic field signals generated by the radial current vectors of the breakdown.

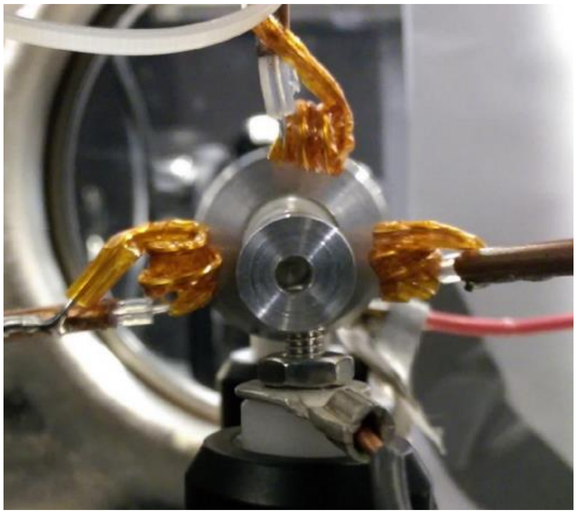

Figure 18: Standard Magnetic field probe placement on CGB machine.

2.3.2.1) Triangulation Technique-Nine Probe Array

The three probe array accurately determines the location of a breakdown about the azimuth of the gap, and hence the centroid of the breakdown current. This array is readily extended to include two additional axial positions (*i.e.* along the current direction through the electrodes), each with three probes to give a total of 9 probes, Figure 19. When applying the triangulation technique for each zone, we are able to map the evolution of the current density over the duration of the current pulse (150 ns) and as the pulse travels along the length of the electrodes (92 mm), effectively tracking the evolution of the current density distribution on either side of the vacuum breakdown in time and space [20].

Figure 19: B-dot array zones labeled on the CGB experiment.

Chapter 2, in part, a reprint of the material as it appears in “Two dimensional triangulation of breakdown in a high voltage coaxial gap” S.W. Cordaro, S. C. Bott-Suzuki, L.S. Caballero Bendixsen, in Review of Scientific Instruments, 86,073503 (2015). The thesis author was the primary investigator and author of this paper.

Chapter 3: Experimental Results

3.1) Initial Results

Early investigation on the CGB experiment shows azimuthal distribution of breakdown in a coaxial gap at a gap size of 900 μm over six shots via end on optical imaging, Figure 20. Subsequent optical measurements at various gap sizes showed similar results, and indicated a reoccurring pattern of asymmetry in azimuthal breakdown.

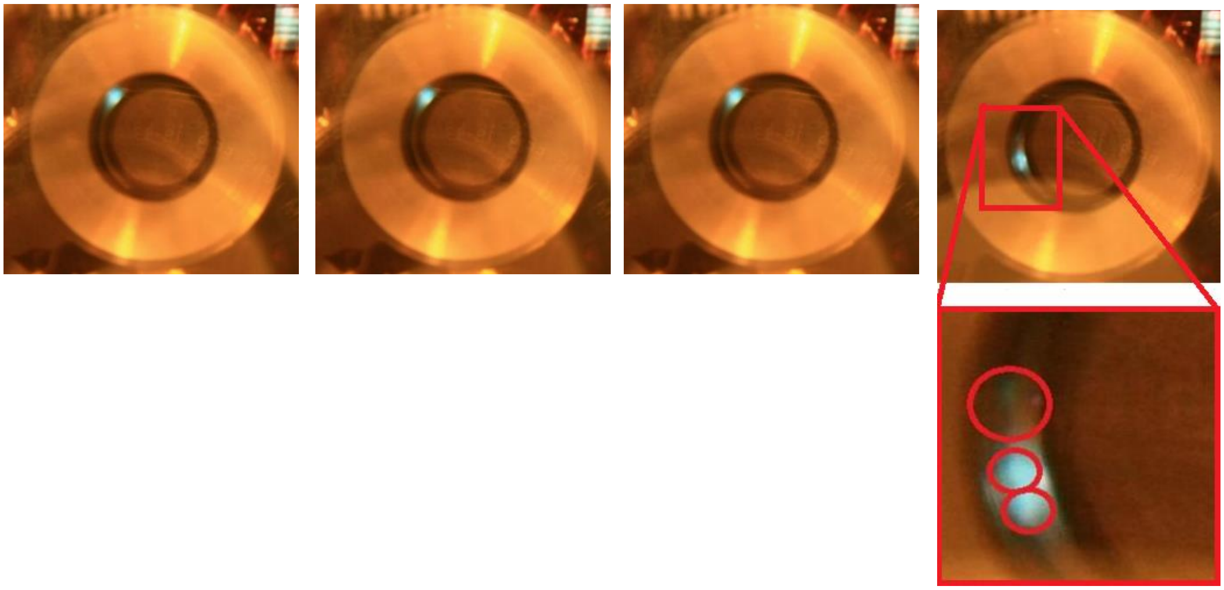

Figure 20: Azimuthal distribution of breakdown in 900μm coaxial gap, over four separate shots.

3.2) Illustration of Triangulation Technique

To illustrate this technique, an analytical calculation of the triangulation method has been performed on a single breakdown occurring at the 90˚ probe side. Each of the three probes is set with at an R value away from the center of the CGB that is measured optically after the shot. Furthermore, it is assumed that all of the current is distributed through the single breakdown point only as shown in the time integrated optical imaging. In order to accurately simulate a current pulse from the CGB, an approximation fit was performed on a typical operating current trace. With this approximated current signal, the peak magnetic field was then calculated using the peak current value and distances the probe center was located from the middle of the breakdown (Table I). The calculated magnetic field values were then used to simulate what the magnetic field trace would look like for each probe (Figure 21).

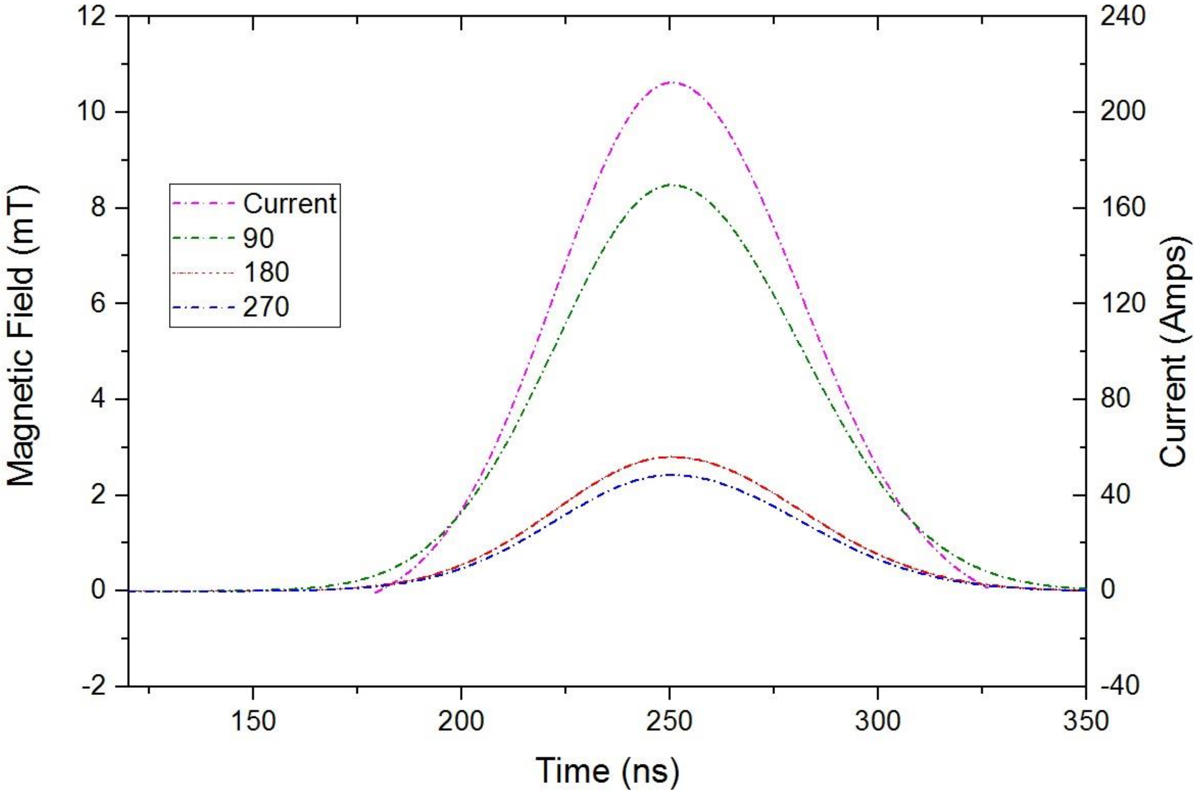

Figure 21: Analytical curves for a breakdown at the 90˚ position.

Table 1: Analytical and measured values of shot no.34

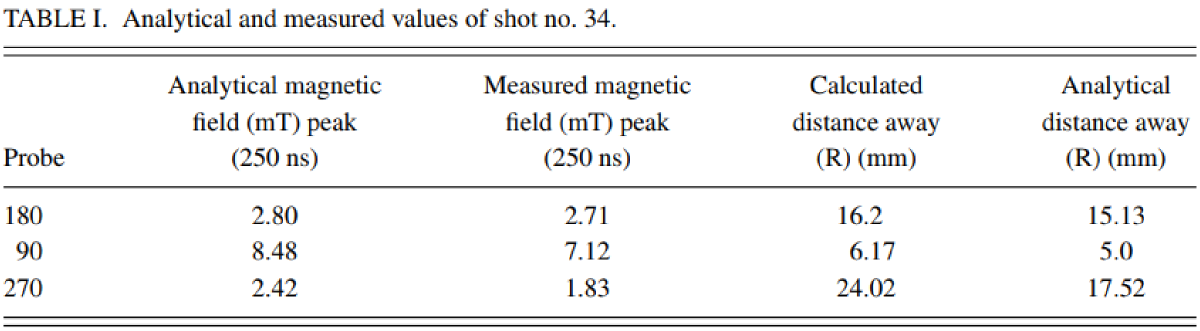

TABLE I. Analytical and measured values of shot no. 34.

Probe	Analytical magnetic field (mT) peak (250 ns)	Measured magnetic field (mT) peak (250 ns)	Calculated distance away (R) (mm)	Analytical distance away (R) (mm)
180	2.80	2.71	16.2	15.13
90	8.48	7.12	6.17	5.0
270	2.42	1.83	24.02	17.52

From Figure 21, it can be seen that the 90◦ probe reads the largest magnetic field, followed then by the 180˚ probe and the 270˚ probe. The analytical probe readings were then overlaid atop experimental probe readings from a shot in which breakdown only occurred at the 90˚ probe side (Figure 22). The resultant figure shows in general that all three probes have the same form and magnitude as analytical calculations, with a maximum error of 13%.

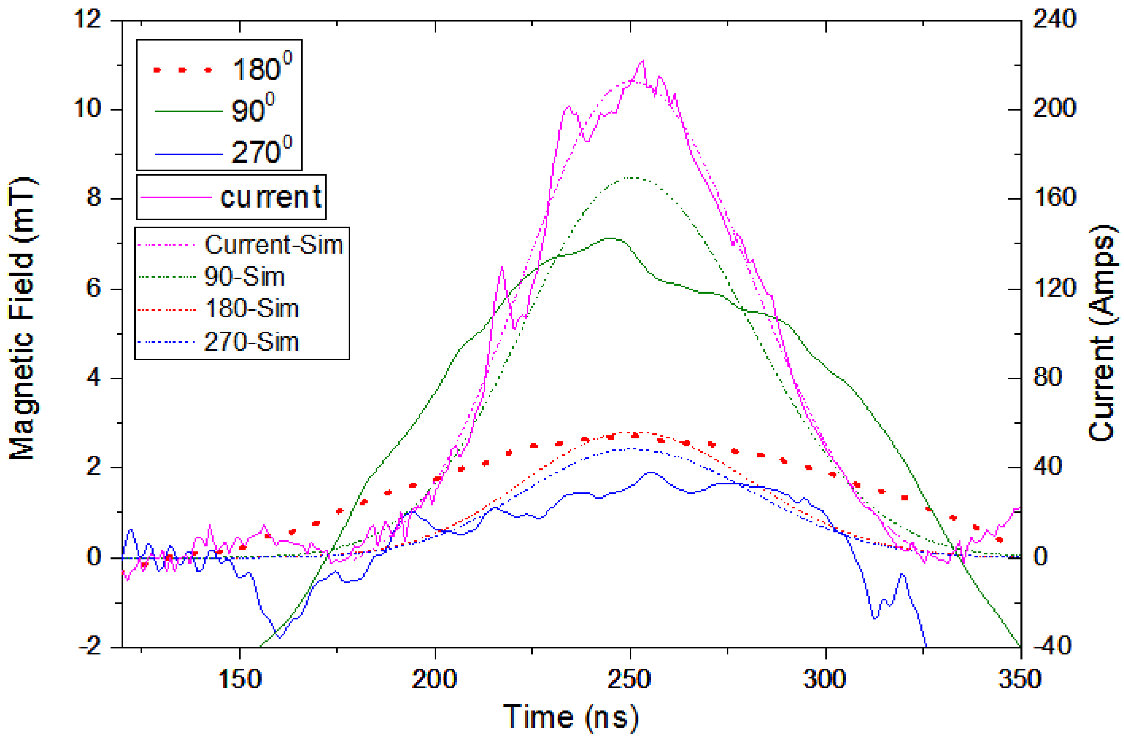

Figure 22: Experimental vs. analytical magnetic field and current, shot no. 34.

The triangulation technique was then performed on the measured magnetic field signals corresponding to shot no. 34, with the calculated distance away from breakdown values in Table I. The corresponding positioning circles were then overlaid atop time resolved optical imaging for the shot (Figure 23) accurately lining up with the exact position at which the breakdown occurred. The differences in distances and peak magnetic field in Table I are not an issue if the probe placement away from the experiment is known from either careful placement or optical imaging before the shot. Furthermore, because these distances are a known quantity, the probe placement about the azimuth is irrelevant as it does not affect the triangulation technique. Though, it should be noted that placing probes closer than 30˚ from one another makes the resultant images more difficult to interpret.

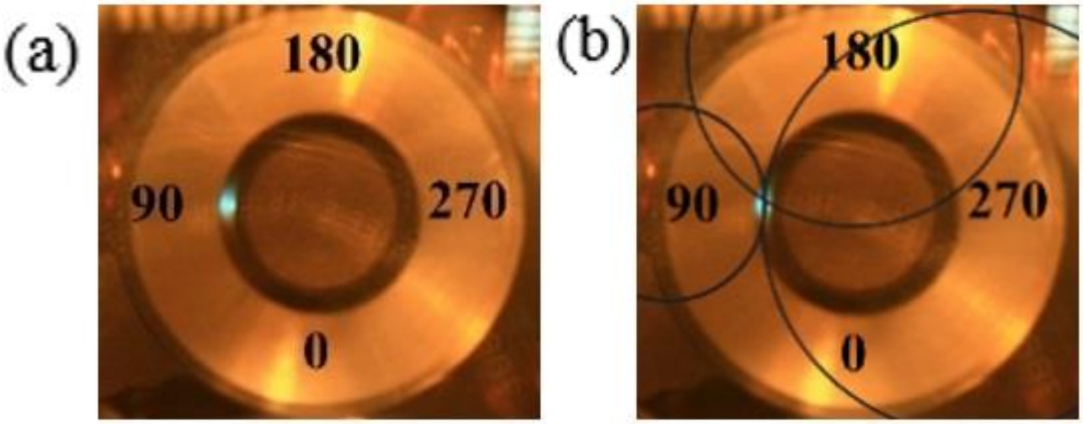

Figure 23: Experimental vs. analytical magnetic field and current, shot no. 34.

The technique is then applied to the signals shown in Figure 24, where the 90˚ probe and 180˚ probe are greater than that of the 270˚ probe. Applying now the triangulation technique to the measured peak magnetic field values, the corresponding distances are found away from breakdown where each probe is located (Table II). With these calculated values, three circles can be generated and overlaid atop their corresponding probe centers in the shot-specific time integrated optical image (Figure 25(b)). As seen from the triangulation cartoon, the centroid of the breakdown was accurately determined by the technique.

Table 2: Analytical and measured values of shot no.45

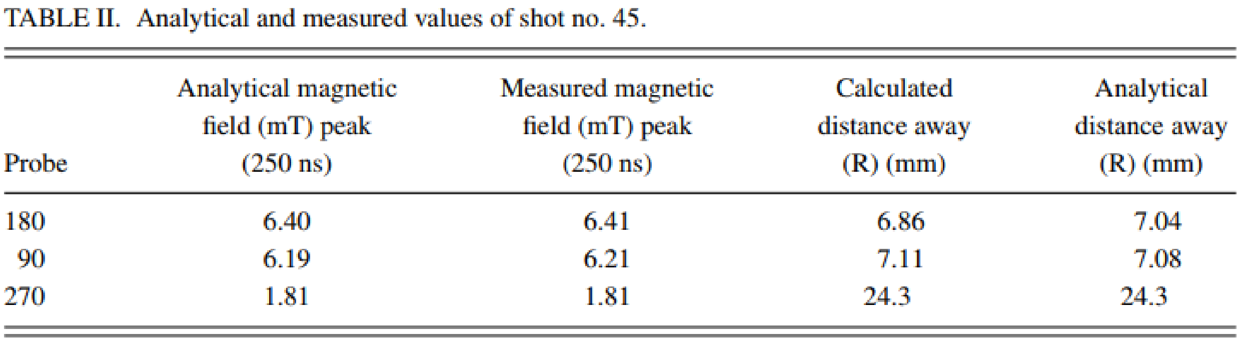

TABLE II. Analytical and measured values of shot no. 45.

Probe	Analytical magnetic field (mT) peak (250 ns)	Measured magnetic field (mT) peak (250 ns)	Calculated distance away (R) (mm)	Analytical distance away (R) (mm)
180	6.40	6.41	6.86	7.04
90	6.19	6.21	7.11	7.08
270	1.81	1.81	24.3	24.3

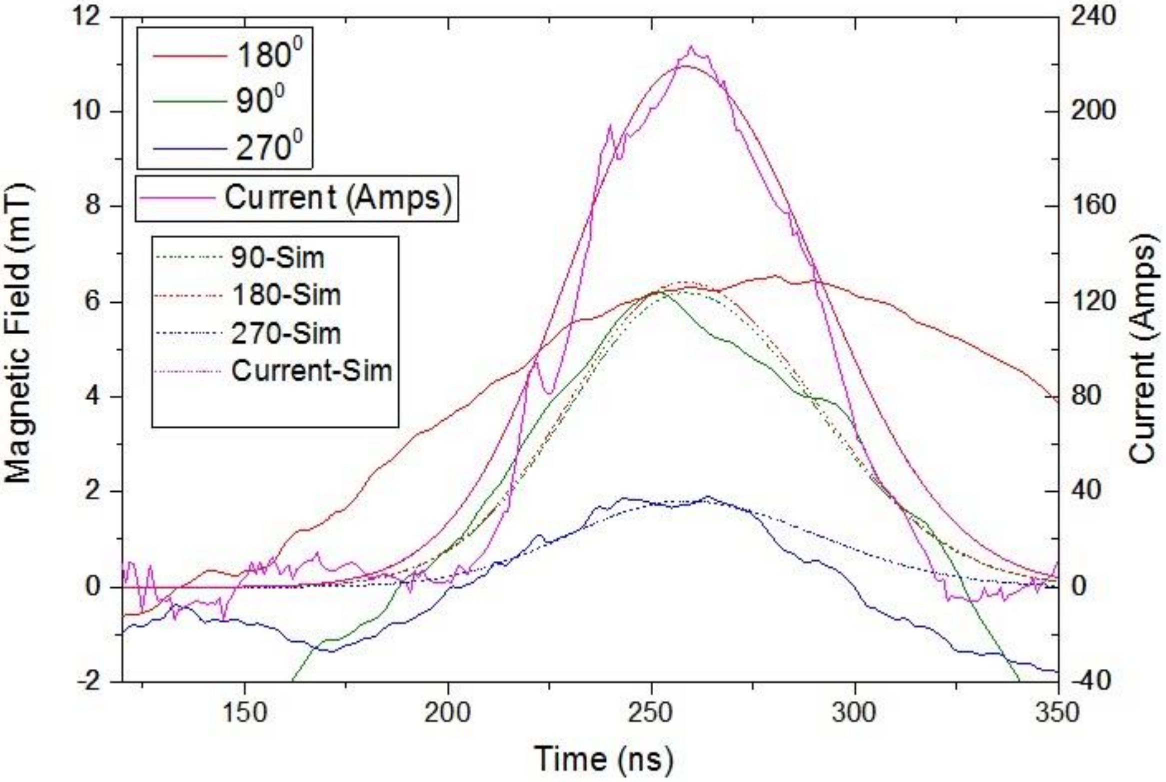

Figure 24: Experimental vs. analytical shot magnetic field and current, shot no. 45.

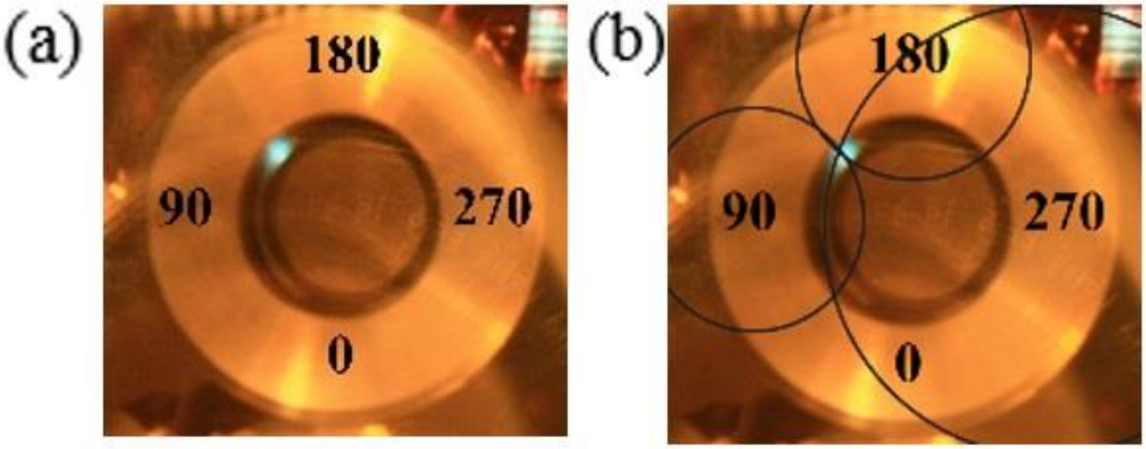

Figure 25: Visualization of breakdown triangulation shot no. 45.

3.2.1) Nine Probe Triangulation

The array geometry used here is given in Figure 26. A set of 3 probes are spaced at 120˚ around the azimuth and separated by 30 mm along the axial direction. The exact location of each probe relative to the electrodes is recoded via the spatially calibrated optical images. The zones are labelled Zone 1 (close to the high voltage connection), Zone 2 (at the position of the coaxial vacuum gap) and Zone 3 (close to the ground connection). Using a triangulation technique for each zone, we are able to map the evolution of the current density over the duration of the current pulse (150 ns) and as the pulse travels along the length of the electrodes (92 mm).

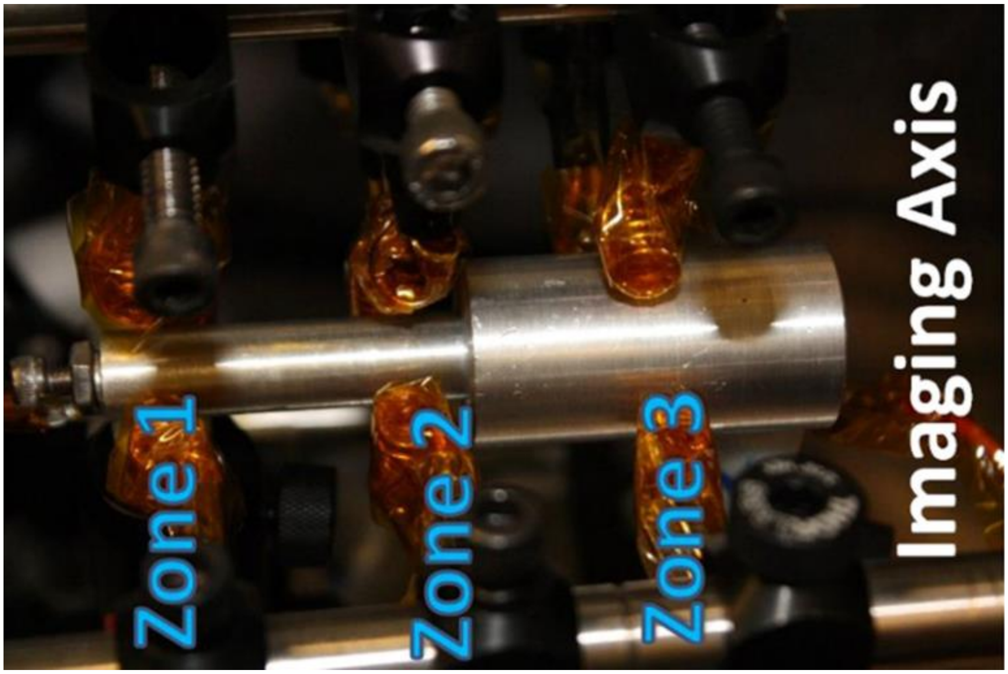

Figure 26: Coaxial gap experiment with b-dot array zones labeled.

To illustrate this, we take the case where a breakdown occurs at the 270˚ position of a 400 μm gap. In Figure 27, the time integrated optical images show the location of the breakdown for this shot, and Fig. 3 shows the raw magnetic field probe data for all probes along with the current trace. Note how the magnetic field probe signal generally follows the trend of the current, and is expected, but with different magnitudes observed between probes at different azimuthal locations. Analysis of the probe data for each zone is carried out using an in-house data analysis program which uses the probe location and the measured field strength to construct a circle of a radius consistent with the total current recorded. A smaller circle for a given probe indicates that, on average, the current density is flowing closer to that probe than one with a larger calculated circle radius. In the ideal case, all probe circles overlap at a single position, as was observed in the previous section. The plots on which the circles are overlaid on the probe position are referred to as triangulation plots.

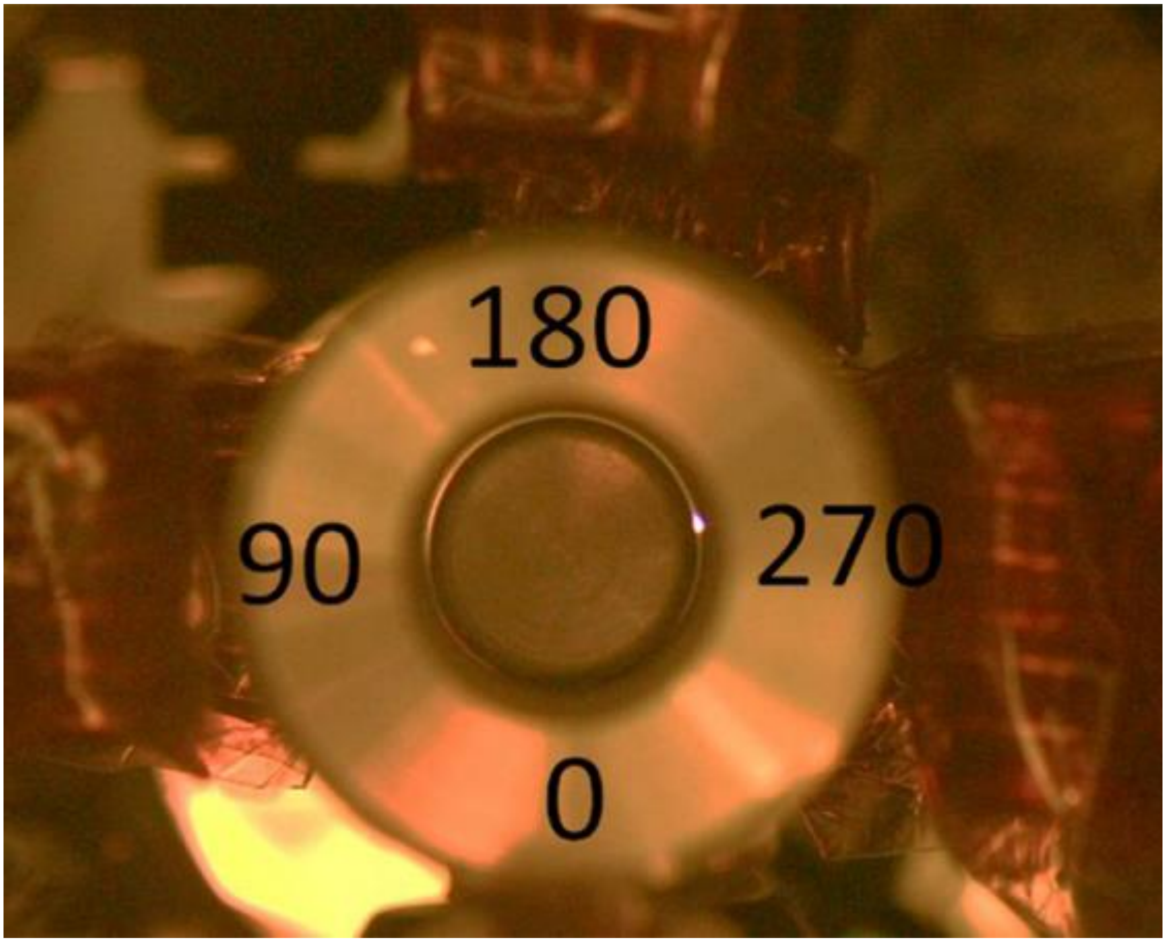

Figure 27: Time-integrated optical image of vacuum gap breakdown for a 400 μm gap, showing the location of the breakdown at 270˚

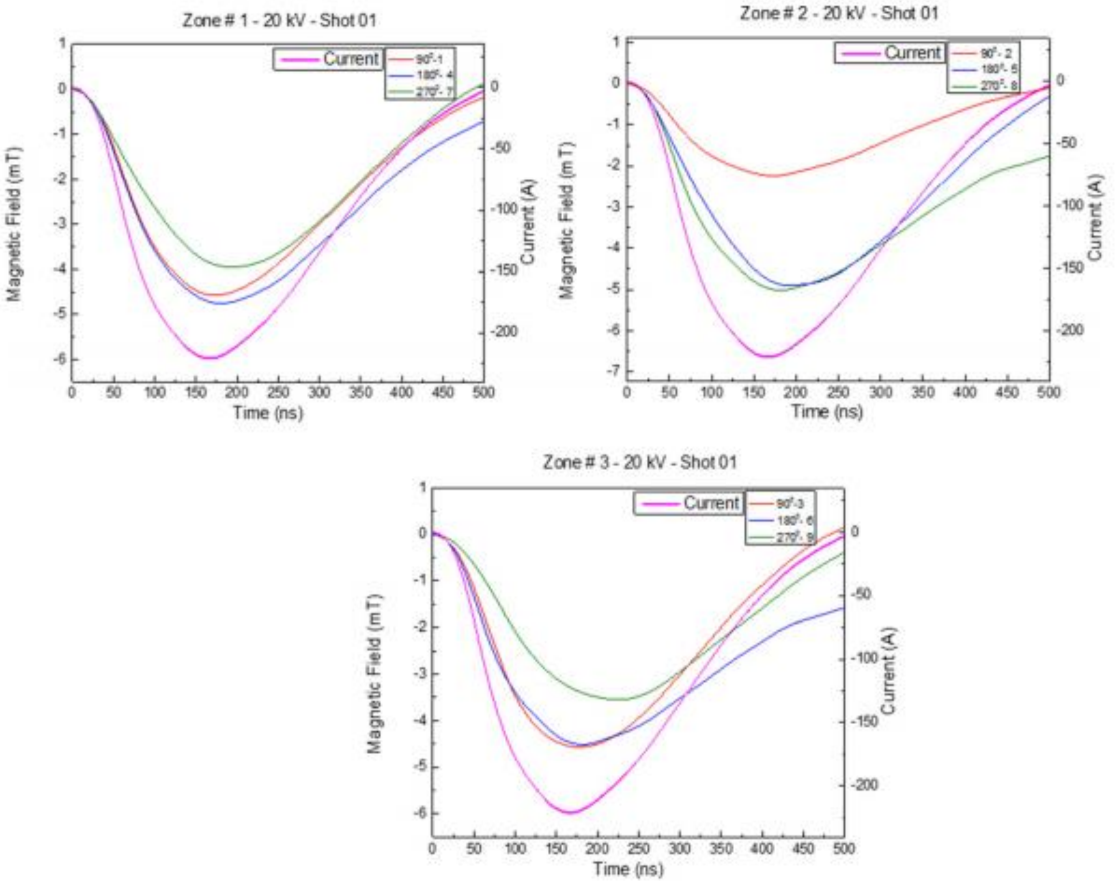

Figure 28: Magnetic field traces, 400 μm gap, Al linear-breakdown at 270˚.

To simplify the analysis for all three zones, triangulation plots are calculated every 10 ns during the current drive and compared to the optical image of the electrodes (Figure 29).

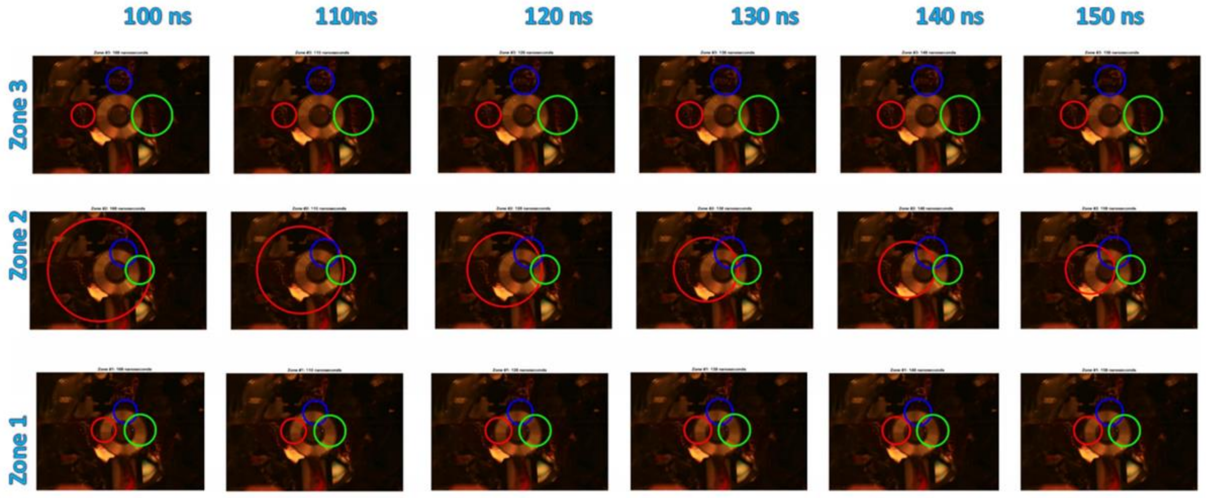

Figure 29: Triangulation matrix, the color of each zone corresponds to the azimuthal position, as in Figure 28. Red-90˚, Blue-180˚, Green-270˚.

The triangulation plots show distinct behaviors between each zone. In Zone 1, 100 ns, the magnetic field probes indicate the current density is in the 90˚–180˚ region, closer to the smaller red and blue circles and further from the larger green circle. In Zone 2, at the same time, the current density has shifted towards the breakdown position at 270˚ (blue and green circles are small, and red ones are large). In Zone 3, the current density returns to the 90˚–180˚ region seen in Zone 1. These distinct offsets remain constant throughout the 50 ns duration as seen in the matrix above. Where the three probe circles overlap at a single position, it is possible to exactly locate the current density. This can be seen, for example, in Zone 2 at 140 ns which corresponds to the optical image location of the breakdown. Often, only an approximate location is possible as outlined here. Which represents some distribution of the current density biased in a particular direction. However, even this highlights significant motion and non-uniformity for different electrode setups.

3.3) Quadrant Mapping

In order to better understand how the magnetic field evolves from shot-to-shot, a method was devised in which the coaxial gap time integrated image is broken into a standard quadrant system with Quadrant 1 always centered at the breakdown position (Figure 30). This simplifies the discussion and accentuates large motions of the average current density position throughout the current drive timescale.

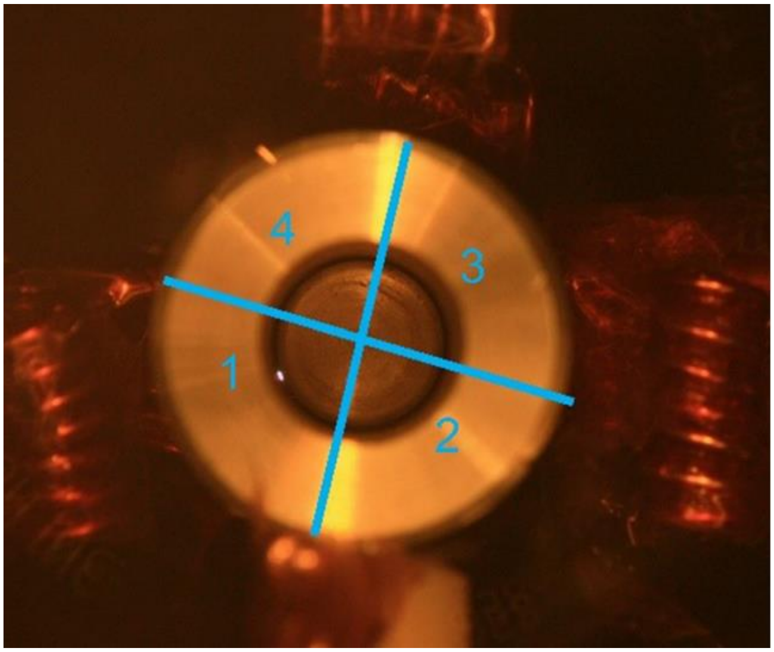

Figure 30: Coaxial gap quadrant overlay; 400 μm, PD-3.03 mm, 25 kV

Combining the quadrant system with the triangulation method yields a quadrant map of the magnetic field evolution, taken at 10 ns intervals during the current drive. Figure 30 shows the result of applying this methodology to a shot with a 400 μm gap and a 3.03 mm penetration depth of the cathode in the anode that has a breakdown around 90. The resulting plot is given in Figure 31.

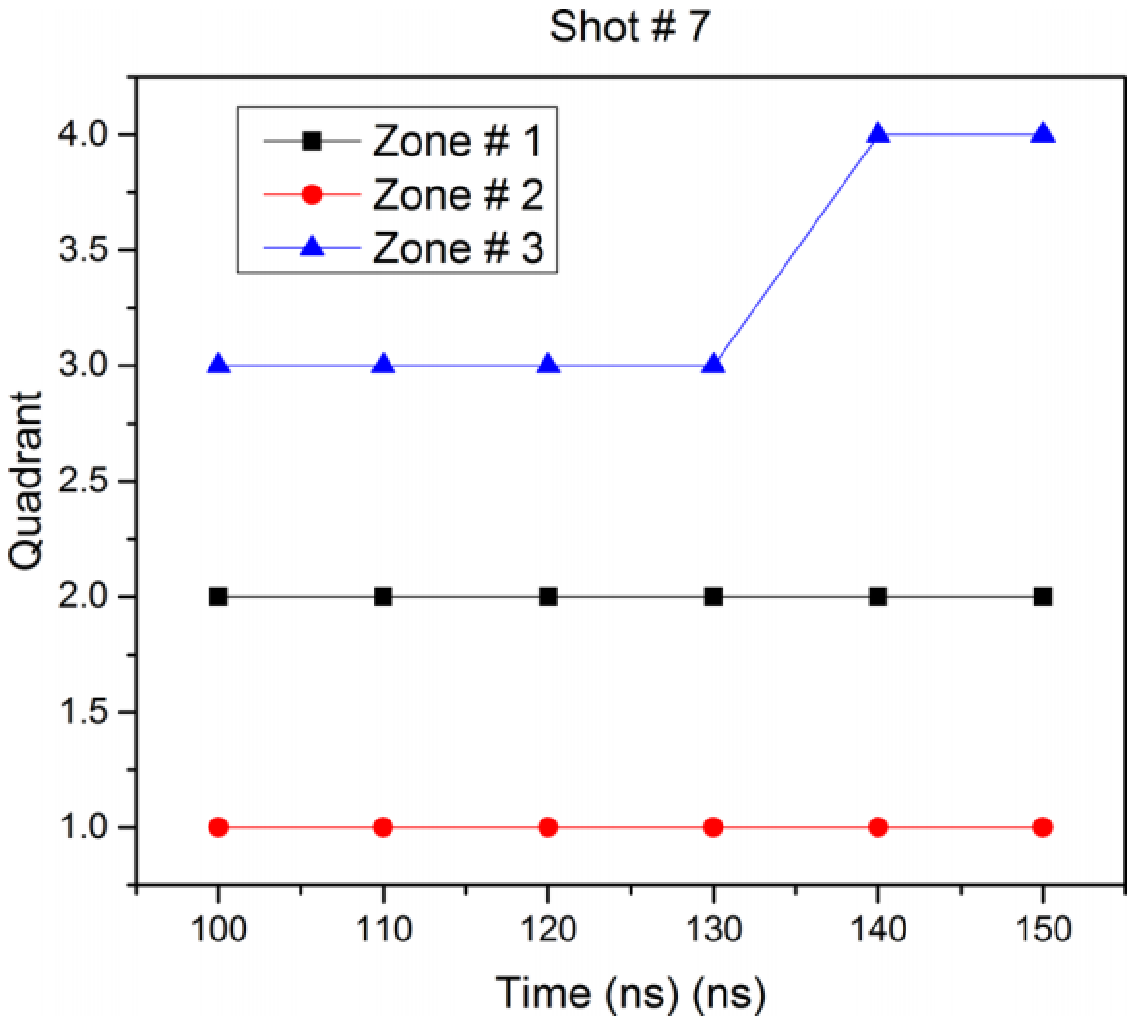

Figure 31: Quadrant mapping, corresponding to Figure 30: note, the use of 1,2,3,4 is chosen since the current distribution is never in say 1.5, it is either in 1, or 1 and 2. Etc.

Zone 2 is the simplest, since this is the location of the breakdown across the gap, and this region is defined as Quadrant 1. Therefore, it can be seen that Zone 2 stays at Quadrant 1 throughout the experiment. In Zone 1, the current density remains in Quadrant 2 from 100 ns to 150 ns. In Zone 3, a transition of the current density from quadrant 3 to quadrant 4 is observed between 130 ns and 140 ns. From this individual quadrant map plot, a persistent offset in current density is observed in the presence of an asymmetrical breakdown in the gap. The motion of the current density observed at locations up and down stream of the breakdown, and does not correspond to its azimuthal location.

3.4) Electrode Penetration Depth Effect on Uniformity

The quadrant mapping was applied to 50 shots in 4 geometries: a 400 μm gap with penetration depths of 3.03 mm and 6.33 mm and a 900 μm gap with penetration depths of 3.72 mm and 9.88 mm. The quadrant mapping method, which shows all 50 shots in this run, also shows a change between the two penetration depths. At PD = 3.03 mm, the current density can occupy any of the 4 quadrants in both Zones 1 and 3. There is also some limited motion between quadrants during the experiment; these are denoted by the horizontal lines between quadrants, and they indicate non-uniformity. It is noticeable that the current density does appear uniform at any time for these shots, even far from the breakdown position (e.g. in Zone 1 or 3 which are 30mm away). When the penetration distance is increased to PD = 6.33 mm, there is distinct difference in behavior. Most notably, transitions in Zone 3 and Zone 1 are constrained to quadrants 3 and 4 in Zone 3, and constrained to quadrants 3, 2 and 1 after 100 ns in Zone 1. Again, there is a persistent changing non-uniformity on either side of asymmetric azimuthal breakdowns over 50 shots and across the length of the electrodes and tens of nanoseconds

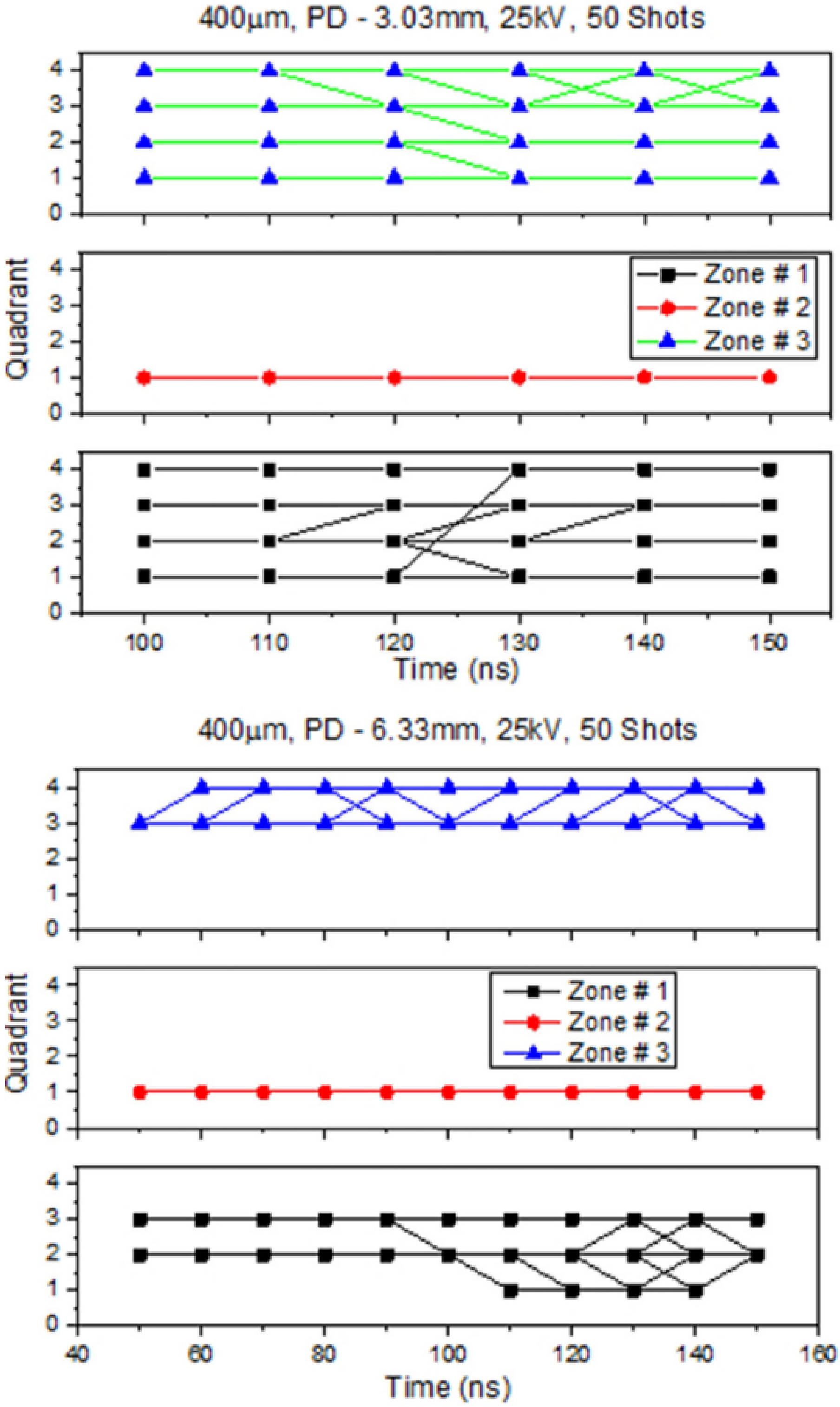

Figure 32: Quadrant maps for 400 μm gaps at different penetration depths.

The results of analysis for 900 μm gap shots are shown in Figure 33. At penetration depths of 3.72 mm and 9.88mm, the quadrant mapping shows several interesting features. Firstly, note that there are now vertical lines for all times examined in both Zones 1 and 3. This denotes that for many shots, the current density was distributed, but not uniformly, around the electrode; i.e., occupying all 4 quadrants at the same time. This was not seen for the smaller gap size. It is important to note here, that at no point in the evaluation of the triangulation matrices for the quadrant mapping (for all shots described in this work) was a perfectly uniform current distribution observed. Additionally, there are more transitions occurring as the current density moves around the electrode. For smaller penetration depths, these occur almost entirely from Quadrant 4 to Zone 1. It appears here that the current density is either uniform or offset close to the position of the breakdown in Quadrant 1. For larger penetration depths, whilst uniform current density is also observed at all times, there is also significantly more motion of the current density between all quadrants. This suggests that the position of breakdown has less effect in influencing the offset of the current density.

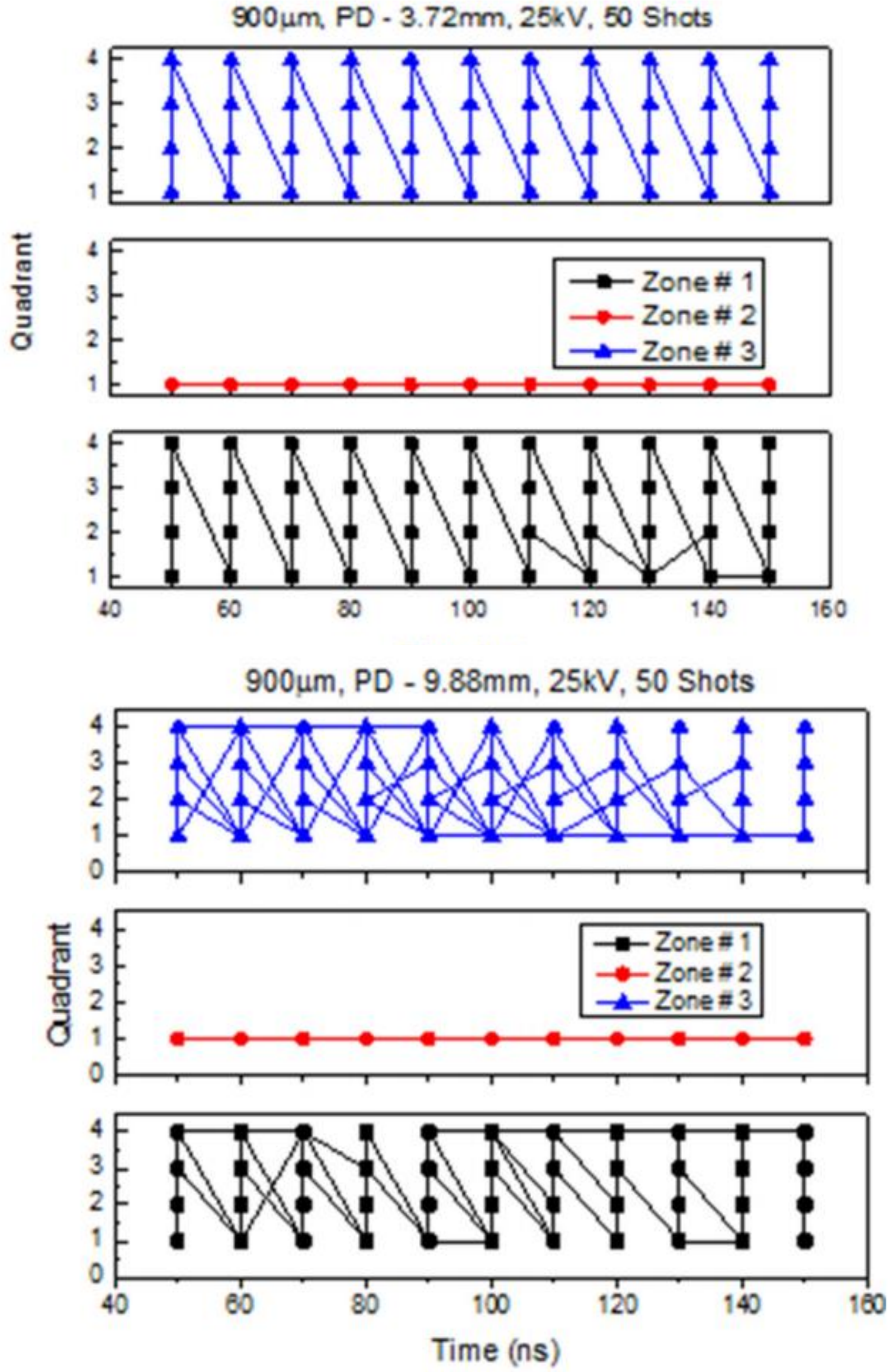

Figure 33: Quadrant maps for 900 μm gaps at different penetration depths.

3.5) Fowler Nordheim Plots-Enhancement Factors

Recovery of electrical data on every shot allows for the characterization of the breakdown process through calculation of the Fowler Nordheim (FN) enhancement factor, as shown in Chapter 1, for each case. This describes the likely breakdown voltage of an electrode set over and above that, expected as a result of the material work function alone. As shown in Chapter 2, the electrodes are unpolished, and so we expect values of the enhancement factor to be relatively large. Following the procedures described in Chapter 1, measurements are taken of the rising edge of the voltage trace before breakdown, These values for each shot are taken and plotted as log $\left(\frac{I}{V^2}\right)$ against $\left(\frac{1}{V}\right)$. The resulting graph yields a line, and the slope of this line gives a value M (Eq. 16) which is a function of the material work function (4.05eV for Aluminum), and the enhancement factor, for that respective geometry. It can be directly examined how the FN enhancement factor changes for our geometries. Figure 34 shows the FN plots for a 730 μm gap at a penetration depth of 2.53 mm, the corresponding enhancement factor is plotted in Figure 35 for three penetration depths.

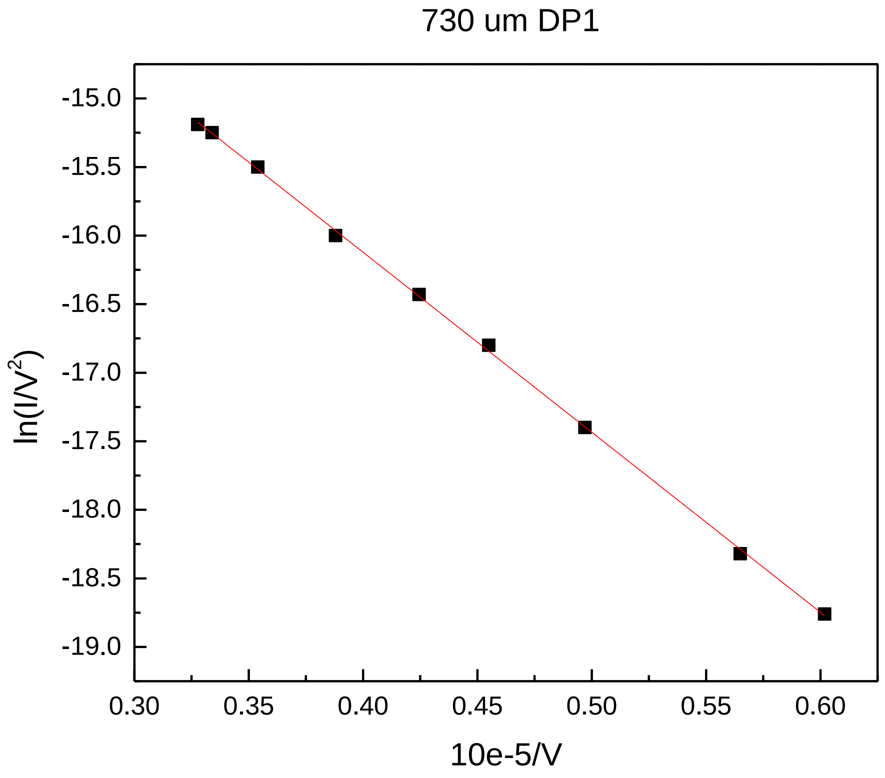

Figure 34: FN plot for 730 μm gap at a penetration depth of 2.53 mm, with linear fit.

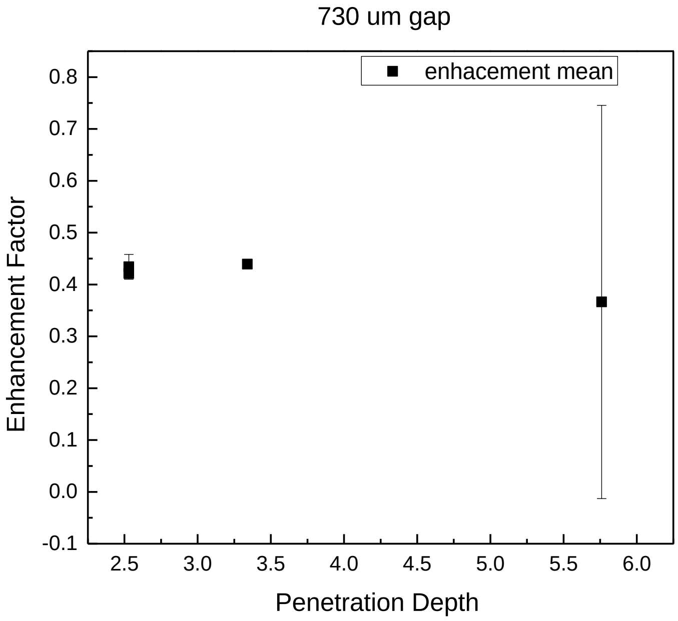

Figure 35: Enhancement Factor for 730 μm gap at various penetration depths.

The enhancement factors shown in Figure 35, are averaged over 50 shots per penetration depth, with error bars show. At first glance, one can see that the enhancement factor changes nominally between 2.53mm and 3.34mm penetration depths, while at 5.76mm penetration depth we see that the enhancement factor varies substantially. At a penetration depth of 5.76mm, 11.5% of the electrodes surface area is inside of the coaxial gap, as opposed to 5.06% (PD=2.53mm) or 6.68% (PD=3.34mm). This significant increase in surface area could be the reason for the extreme variation of the enhancement factor. When inspecting optical images for each penetration depth, no noticeable difference can be discerned. A more in-depth comparison is made in the next section.

3.6) Comparison of Enhancement Factor and Quadrant Mapping

The quadrant mapping technique and the F-N analysis were applied to 50 shots in each of 5 geometries: a 400 μm gap with penetration depths of 3.03 mm and 6.33 mm and a 900 μm gap with penetration depths of 3.72 mm and 9.88 mm, as well as gaps of 330 μm, 730 μm, and 1150 μm at penetration depths of 2.53mm (DP1), 3.34mm(DP2), 5.76mm(DP3). The corresponding graphs are presented below.

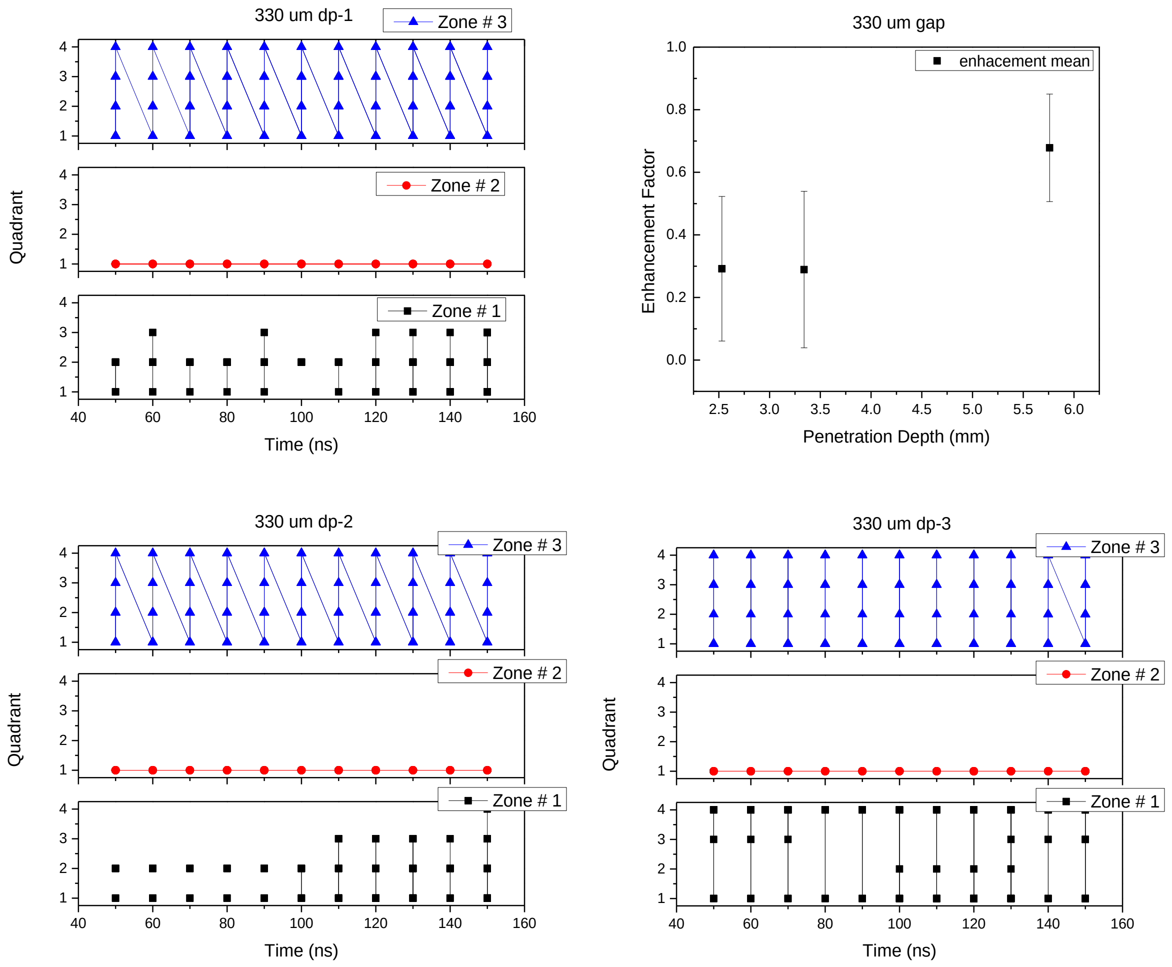

Figure 36: 330 μm gap FN and Quadrant maps

Figure 36 shows the FN and quadrant analysis for a 330 μm gap at three penetration depths. For DP1 we see that the enhancement factors is on average 0.291$\pm$0.230(V/A)eV, as we increase to DP2 we see the average enhancement factor decreases slightly 0.289$\pm$0.250(V/A)eV. Upon increasing to DP3, we see the enhancement factor increases to 0.678$\pm$0.171(V/A)eV, which is twice as large as the first two penetration depths. When considering the quadrant map we note that as in our initial quadrant mapping covered in 4.5 for the 900 um gap, we see vertical lines and horizontal lines here in each of our depth penetrations. It is especially interesting when we first compare DP1 and DP2—in addition to the similar enhancement factors for each—we see that the quadrant mapping for each are also remarkably similar. Both exhibit a full distribution among quadrants in Zone 1, which shows a (1,2) quadrant asymmetry that dominates in early time that branches into quadrant 3 late time and quadrant 4 for full quadrant distribution at peak current rise time (150ns). In addition both have a zone 3 that is identical, with probability of distributing current in all four quadrants but not uniformly every shot, as indicated by the horizontal transition lines.

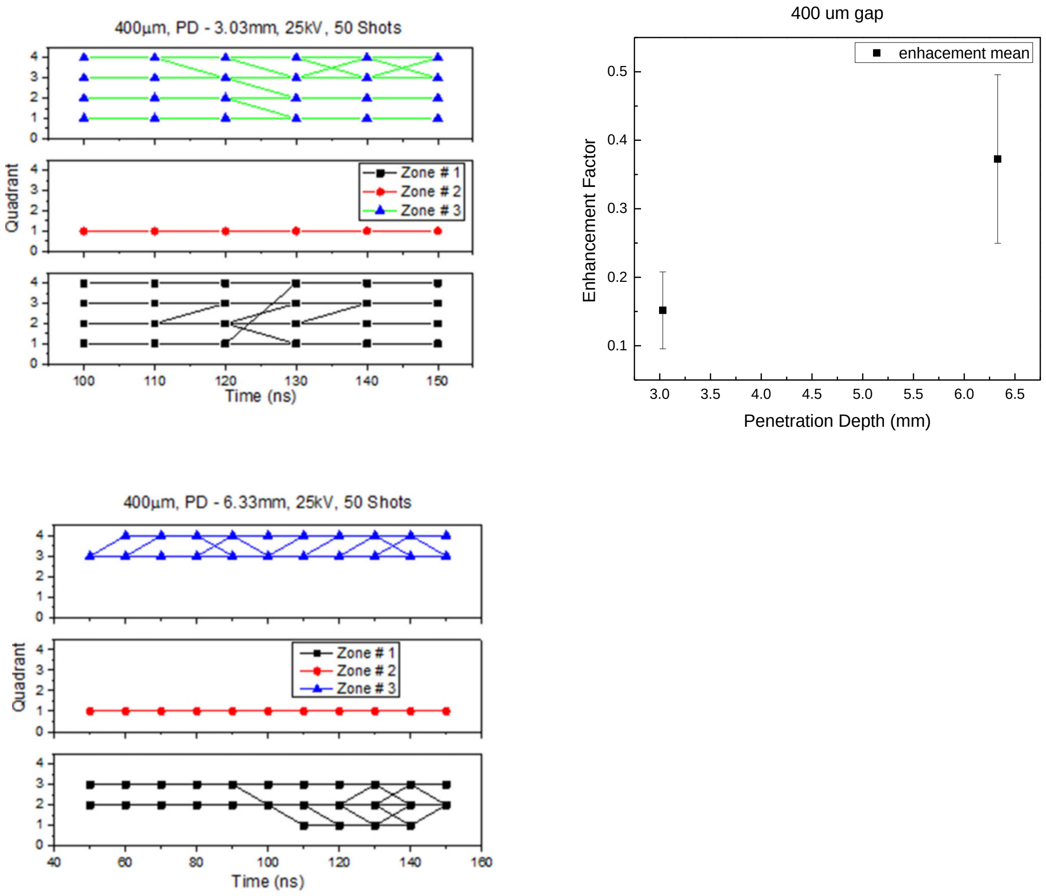

Figure 37: 400 μm gap FN and Quadrant maps

Figure 37 shows the variation in both the enhancement factor and the quadrant mapping resulting from the change in the penetration depth from 3.03 mm and 6.33 mm for a 400 lm gap. For the smaller penetration depth, we see an average enhancement factor 0.152± 0.056 (V/A)eV with the larger depth being, on average, 0.373 ±0.123 (V/A)eV. This is a difference of a factor of 2.45. The quadrant mapping method, which shows all 50 shots in this run, also shows a change between the two penetration depths. At PD = 3.03 mm, the current density can occupy any of the 4 quadrants in both Zones 1 and 3. There is also some limited motion between quadrants during the experiment. It is noticeable that the current density does not look uniform at any time for these shots. When the penetration distance is increased to PD = 6.33 mm, there is distinct difference in behavior. Most notably, transitions in zone 3 and Zone 1 are constrained to quadrants 3 and 4 in zone 3, and constrained to quadrants 3, 2 and 1 after 100 ns in Zone 1. Again, there is a persistent changing non-uniformity on either side of asymmetric azimuthal breakdowns over 50 shots and across the length of the electrodes and tens of nanoseconds.

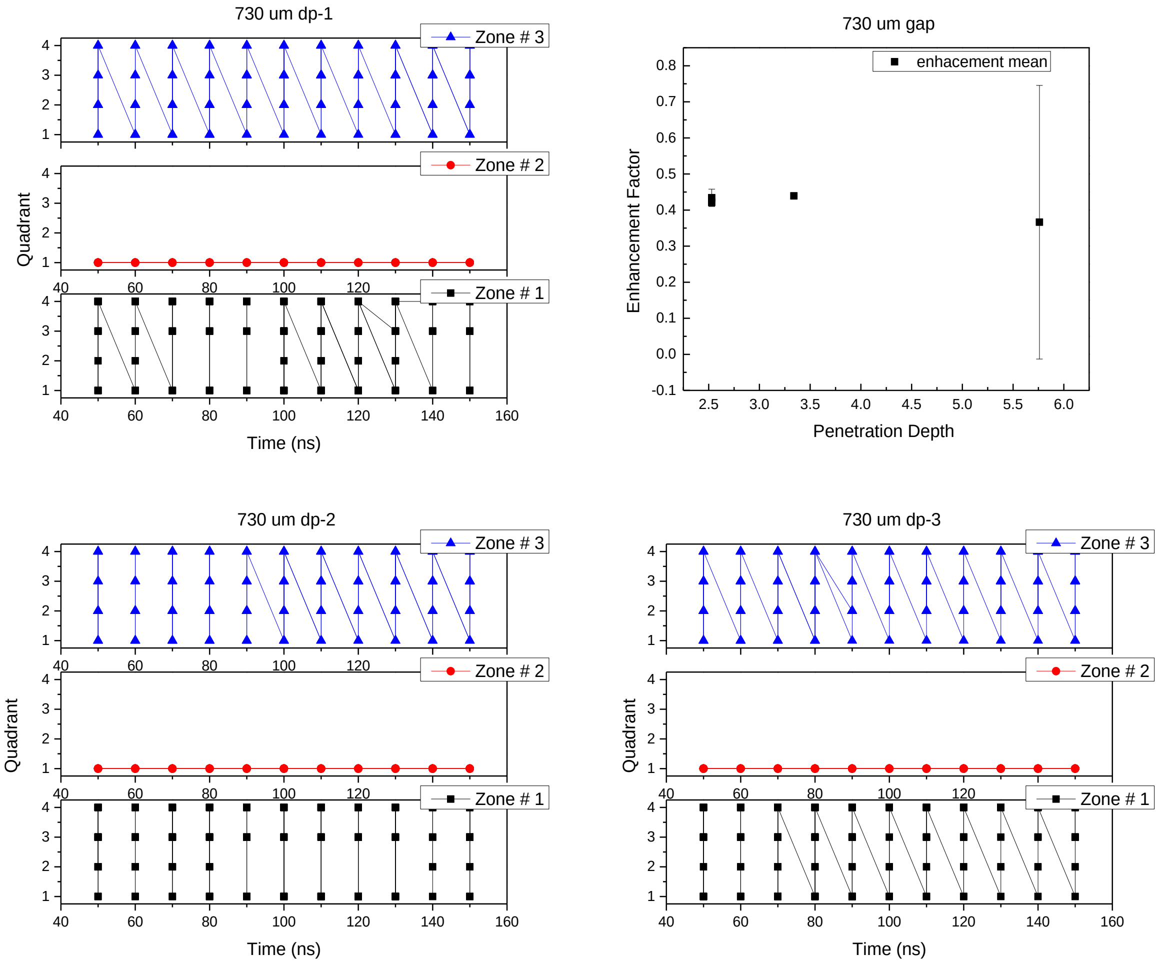

Figure 38: 730 μm gap FN and Quadrant maps

Figure 38, shows the resulting analysis for 730 μm at the three penetration depths. For DP1, we see that the enhancement factor is on average, 0.434± 0.0238(V/A)eV. As we increase to DP2, our enhancement factor barely changes, only increasing to an average of 0.439 (V/A)eV, with no marketable deviation over 50 shots. Increasing to DP3, we see an average decrease to

0.366±0.379 (V/A)eV, with a standard deviation more than the average enhancement factor. When looking at the quadrant mapping for this shot, one can immediately notice some interesting behaviors. For DP1, DP2, and DP3 zone 3 shows a persistent distribution about all the quadrants for all shot. When looking at Zone 1 for all shots, we see that both DP1 and DP2 have current asymmetries around 80-90ns, before returning to current distributed in all quadrants. Where as in DP3, Zone 1 has current distributed about all 4 quadrants for the duration of the current pulse.

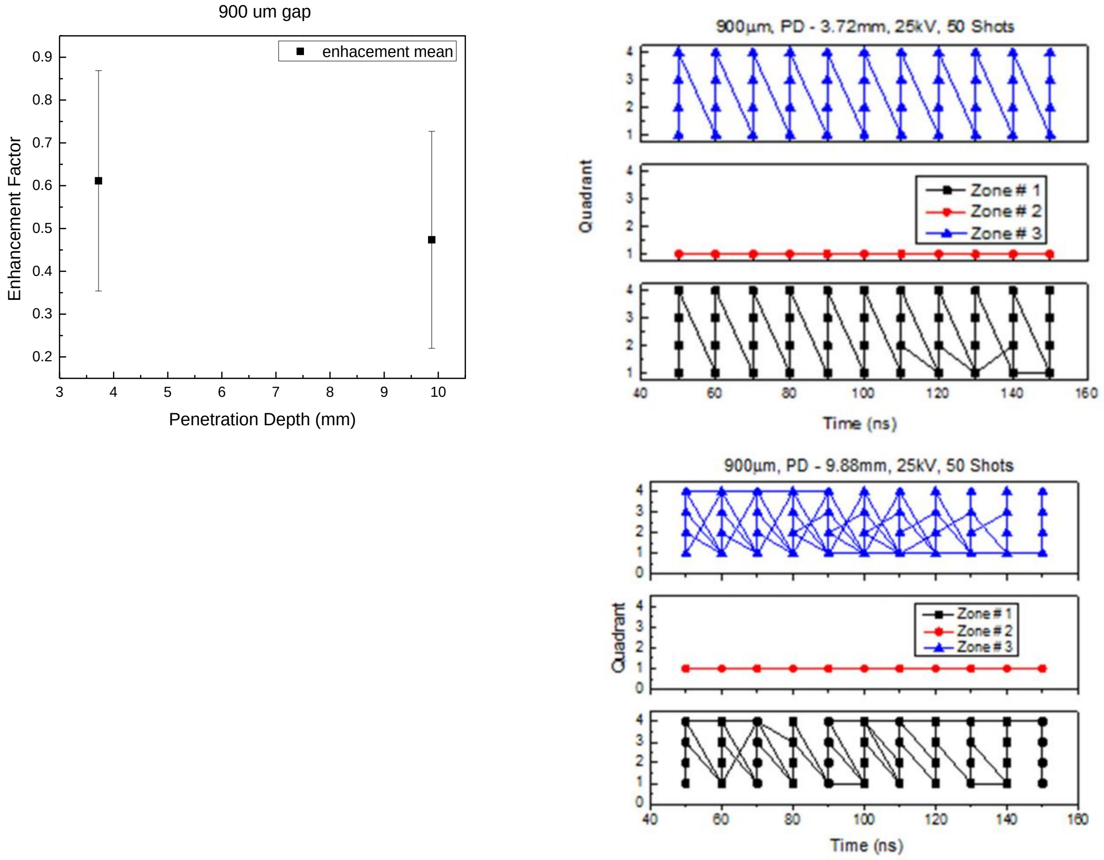

Figure 39: 900 μm gap FN and Quadrant maps

The results of analysis for 900 μm gap shots are shown in Figure 39. At penetration depths of 3.72 mm, the enhancement factor has an average value of 0.6113± 0.257(V/A)eV, several times smaller than the factor for the 400 μm gap shots at similar depths. When the penetration depth is increased, however, the variation in the enhancement factor is very small, with and average value of 0.473± 0.253 (V/A)eV. This is similar to the values of the larger penetration depth for smaller gaps. The quadrant mapping shows several interesting features. Firstly, note that there are now vertical lines for all times examined in both Zones 1 and 3. Additionally, there are more transitions occurring, as the current density moves around the electrode. It appears here that the current density is either uniform or offset close to the position of the breakdown in Quadrant 1. For larger penetration depths, whilst uniform current density is also observed at all times, there is also significantly more motion of the current density between all quadrants. This suggests that the position of breakdown has less effect in influencing the offset of the current density.

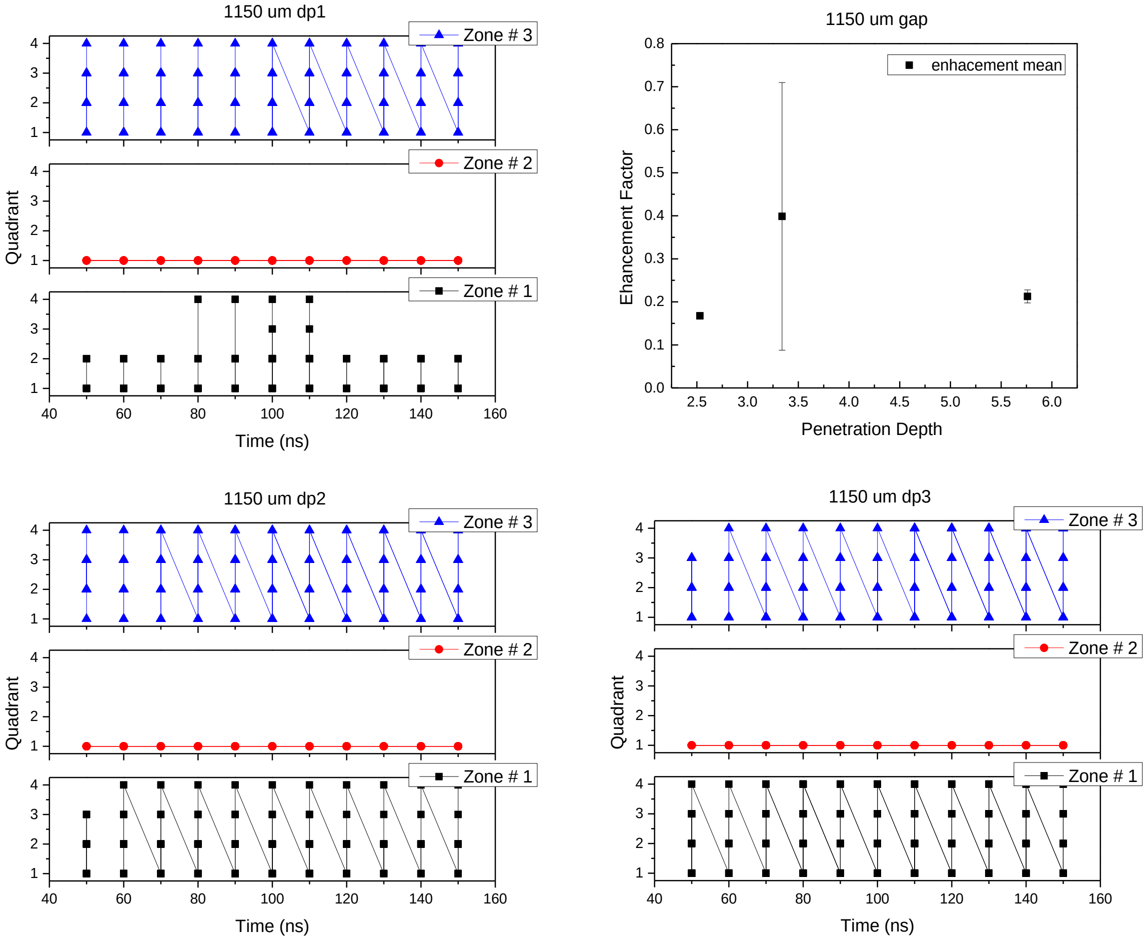

Figure 40: 1150 μm gap FN and Quadrant maps

Figure 40 shows the final gap size FN and quadrant map analysis. We can see that at DP1 we have an enhancement factor of 0.167± 0.00736(V/A)eV, with a very small standard deviation. As we increase to DP2, we have a stark increase of enhancement factor to 0.398 ± 0.310(V/A)eV, with a large standard deviation. As we increase to DP3, we have a decrease in enhancement factor of 0.212± 0.015(V/A)eV. Upon inspection of the quadrant mapping we immediately see a difference between the three penetration depths. Notably, when looking at Zone 1for DP1 we see asymmetry that persists throughout the duration of the shot, with a 20 ns interval in which the current distributes to all quadrants. For DP2, and DP3, we see similar distributions and movement across all zones.

Chapter 3, in part, a reprint of the material as it appears in “Time and Space resolved current density mapping in three dimensions using magnetic field probe array in a high voltage coaxial gap” S.W. Cordaro, S. C. Bott-Suzuki, in the Journal of Applied Physics 122, 213303 (2017). The thesis author was the primary investigator and author of this paper.

Chapter 4: Conclusions and Beginnings of a Pseudo-Analytical Framework

Through experimentation on the coaxial gap breakdown machine, we have been able to answer many of the questions set out in the beginning of this text. The answers to these are outlined below.

4.1) Mechanisms of Breakdown

The electrodes used in this experiment have a surface finish on order of ~5-10μm as shown in Scanning Electron Microscope (SEM) surface profile images (Figure 11 (a, b)). The electrodes are cleaned, but not polished or treated. This surface finish indicates points for increased field enhancement. This also allows for the electrodes to fall into the regime of one of the assumptions we have made in Chapter 1 on Cold Field Enhancement, that the emitting surface is rather smooth, such that irregularities are small (<10-20$\mu m.$) compared to the width of the potential barrier (gap size).

The electrodes are under vacuum (~10^5 $Torr$), and subject to 25kV, 240A-150ns. This indicates that the electrodes are at room temperature, and not subject to any resistive heating due to the short current pulse and relatively low current. This puts the emitting metal surface in the regime of our Cold Field Enhancement approximation, of T ~ 0K.

With the last two approximations in Cold Field Enhancement being purely mathematical constructs to allow for closed solutions as found in Chapter 1, we can say that our experiment, and the mechanisms causing the breakdown of our coaxial gap are well described by the Cold Field Enhancement Theory.

4.2) Persistence of Asymmetry in a Coaxial Gap

In this text, we have shown that asymmetries in the azimuthal breakdown position have an influence on the asymmetric current distribution in time and space. These asymmetries in current density can be influenced by changes in the gap size and the penetration depth, and have been measured experimentally as a function of time and space by use of the 9-probe triangulation technique and quadrant mapping, as shown in Chapter 3. It is important to note, that at no point in the experiment does the current density become completely uniform, even when all probes indicate current is in all quadrants for any of the gap sizes or penetration depths. This can be seen if we look back at Figure 29, specifically at Zone 1,3 at 150ns. We see that the probe circles are in all quadrants but the radii of the circles are different by many percent, which indicates non-uniformity.

4.3) Enhancement Factor Correlation to Gap Size and Current Distribution

Looking at Figure 41 we can see that for gaps 400, and 330, we have an increasing average enhancement factor as we increase in penetration depth greater than 3.34 mm. For 730, 900, and 1150 um gaps we see an increase in average enhancement factor before 3mm and a decrease after 3.34mm. If we plot field enhancement versus gap length for each penetration depth, we can see a “global” trend. In DP1, as gap length increases, enhancement factor increases until the gap size exceeds $900\mu m$. In DP2, again we see a similar trend, an increase in field enhancement as gap size increases until the gap size exceeds $900\mu m$. In DP3, we see an overall decrease in field enhancement factor as gap size increases.

When correlating enhancement factor to asymmetry growth or decay, it is not very straight forward to say anything definitively. Some interesting features are useful to point out, that occur after a penetration depth greater than 3.34mm occurs. In the 330 μm gap we see that Zone 1 becomes noticeably more distributed about all four quadrants. In the 400 μm, zones 1,3 become significantly less uniform. In the 730 μm Zone 1 becomes significantly more evenly distributed, with no distinct asymmetries. For the 900 μm we see an increase in asymmetry of current distribution in Zone 1,3. For 1150 μm we see no real change in current distribution. In order to better understand these results, a more in depth study is required, and will follow.

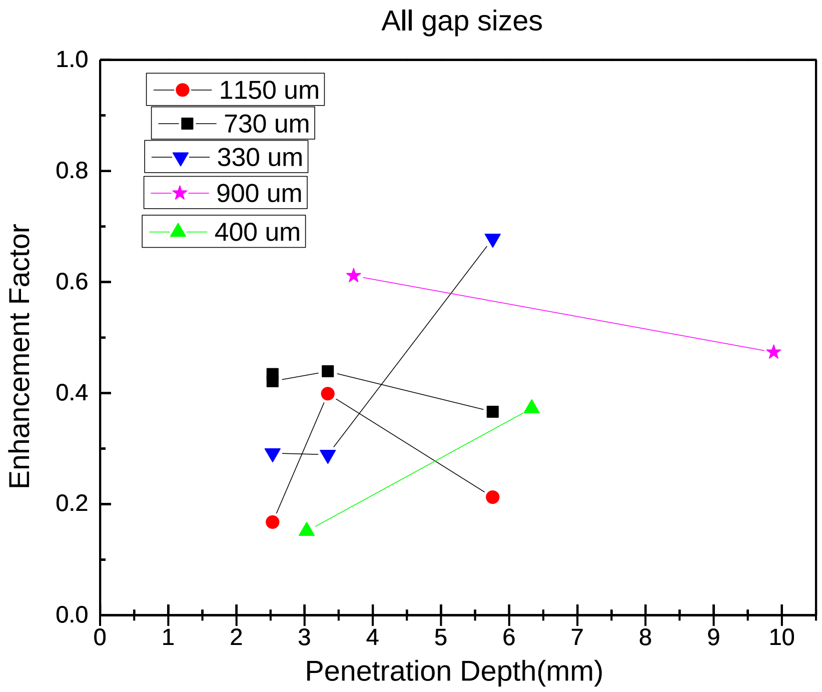

Figure 41: Enhancement Factors for all gap sizes

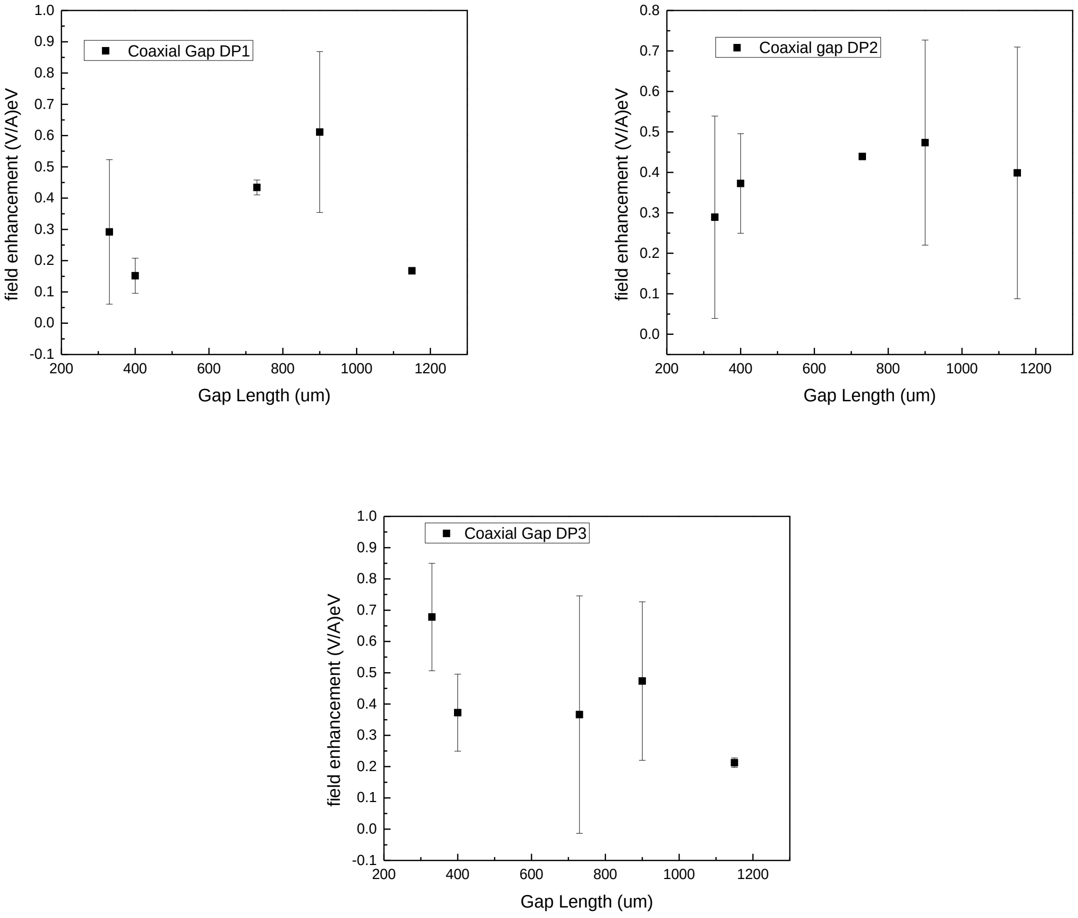

Figure 42: Enhancement Factors for all gap sizes

4.4) Comparison to Previous Work

To see where this work stands with similar geometries, we compare to the work by M. Okawa presented in Chapter 1. Firstly, to get the graph into the proper form for comparison we must take into account that M. Okawa used mm size gap sizes as well as not using the form factor used in the Fowler Nordheim approach also described in Chapter 1. This amounts to dividing our gap length by one thousand, and multiplying our y-axis by one thousand. The result is shown in Figure 43.

Figure 43 shows a few interesting similarities between the coaxial gaps in each penetration depth and the data from M.Okawa on the listed geometries. It is readily seen that the coaxial gap data for all penetration depths is larger in field intensification than any of the listed geometries. This could be caused by the increased surface area in the coaxial gap coupled with the significantly smaller gap length. The field intensification generally increases as the gap length increases. When constrained to DP1 and DP2, the field intensification magnitude is most similar to Ring-Ring and Sphere-Sphere geometries. The trends seen in the Cylinder-Plane geometry slightly decreases in intensification factor as gap length increases is also seen in DP3. These similarities would indicate that the coaxial gap field intensification factors are well within the appropriate regime, and add to the existing data.

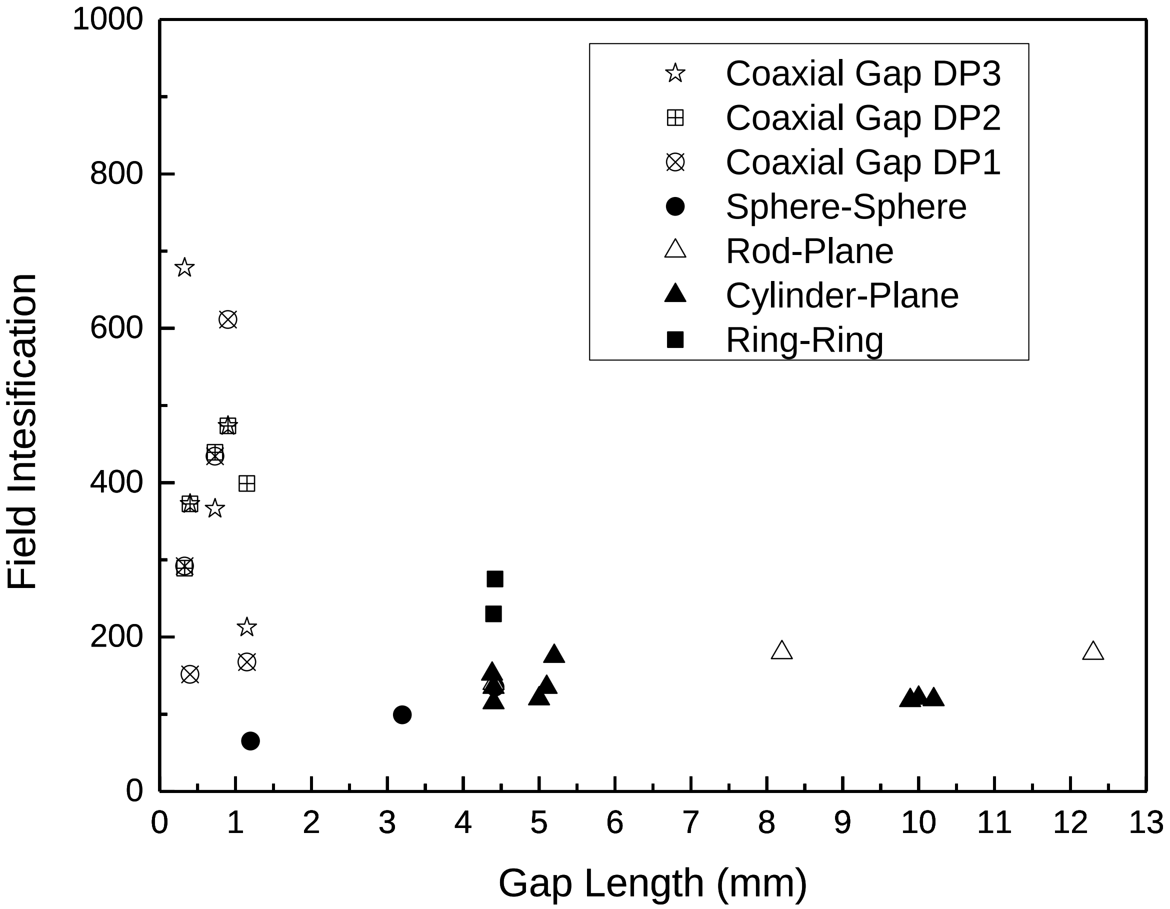

Figure 43: Enhancement Factors for all gap sizes

4.5) Application to Sandia Z-Machine

Recalling the findings in Chapter 1.6, the equation of motion for the liner was found (8). Expanding on the 1-D pseudo-analytical derivation and combining results of asymmetry in current distribution in the coaxial gap (liner), it can begin to be understood how these effects might cause issues. Assuming that the vacuum gap for a MagLIF experiment breaks down in a similar way to the observation in our experiment, the current density will be non-uniform around the liner surface (in the azimuthal direction). Our results show that non-uniformity can persist 30mm from such a breakdown, which is much longer than liner height, and so the liner is driven non-uniformly.

To begin, mirror the 2-D image and the 1-D model about the y-axis as shown in Figure 45. From here, the data presented in Chapter 3 on the asymmetries found in a coaxial gap is applied to our simplified z-liner image to calculate the acceleration of the liner (2.5.8).

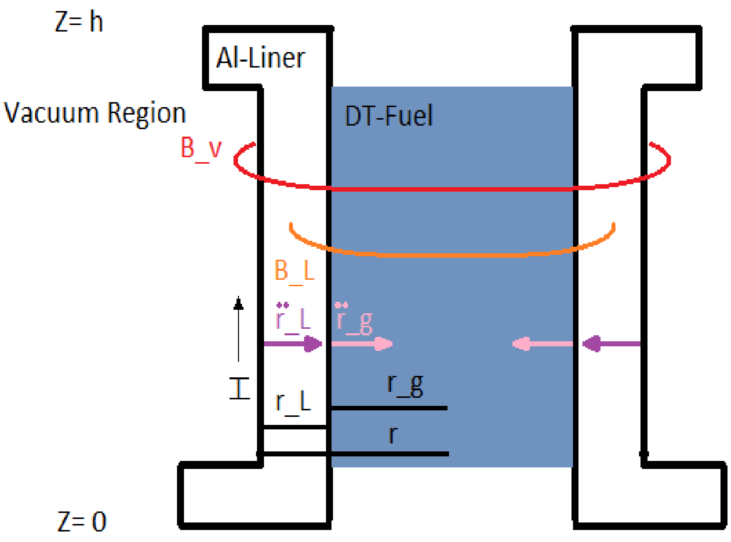

Figure 44: 2-D slice of the Z-liner

The following experimental and idealized parameters [20-24] presented in Table 3, as well as a current split across the load from the right hand side it is 44% of the total, and 56% from the left hand side for an example, are used to calculate the liner acceleration. It is important to note that only the acceleration of the liner is considered, since it is the only equation of motion that is dependent on current, as well as taking current magnitude to be that of peak current. The resultant values are presented in Table 4.

Table 3: Experimental and Idealized parameters for the MagLIF experiment.

Applied Axial B-Field	Total Peak Current	Liner Radius	Fuel Radius	Fuel Pressure	Liner outer Radius	Mass density Liner	Liner Pressure	Liner Height
30 T	18 MA	0.465mm	2.325	3GBar	3.48mm	428 mg/cm	2.4 MBar	7.5mm

Table 4: 1D calculation, asymmetric current.

	Left Hand Side	Right Hand Side
Liner Acceleration: $\ddot{r}_l$	$3.75x10^9 \frac{m^2}{s^2}$	$2.24x10^9 \frac{m^2}{s^2}$

When looking at Table 4, it is readily apparent that the LHS accelerates inward 67% faster than the RHS, and this is only with a 4% difference in current from LHS to RHS. This result can be exaggerated if the current considered in the MagLIF experiment has more wildly varying current percent differences between the LHS and RHS as was observed in Chapter 3 for the CGB experiment. The results are shown in Figure 44, for current percent differences ranging from 1% - 56%.

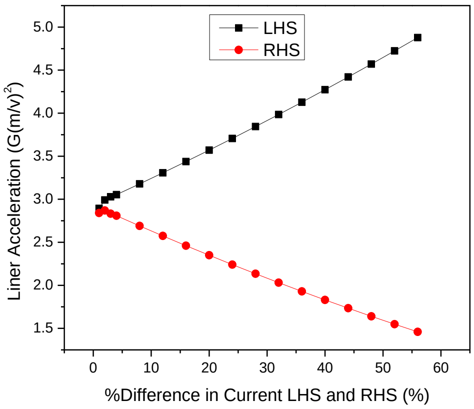

Figure 45: Liner acceleration for various % Current differences.

If the MagLIF experiment follows a similar trend of having asymmetries throughout the duration of the current pulse—even with percent differences as small as 1% from the LHS and RHS—the LHS will still accelerate 1.73% faster than the RHS. If the behavior of the current is similar in the MagLIF experiment as to the CGB experiment, asymmetric acceleration due to asymmetric current density distribution could prove detrimental to the overall success of the liner compression phase due to its strong dependence on current symmetry, which has been shown in the CGB machine to never be uniform. However, it is important to note that the liner compression phase is stabilized by the gas compression phase because of the pressure in the fuel and the external applied axial field.

4.6) Final Thoughts

Future studies will focus on extended parameter scans of the gap size and the penetration depth, as well as increasing the current to see how the technique scales with mega ampere currents and above. Further studies will also include electrode materials and surface imaging before and after shots to determine the change in the FN enhancement factor as a function of breakdown surface area. Finally, a computational model will be developed to describe and analytically determine the method for asymmetric distribution of current as a probabilistic distribution function. Once a three dimensional computational model has been accurately created, re-applying them to MagLIF level currents and gap sizes will likely yield detailed information pertaining to liner compression asymmetry.

Chapter 4, in part is currently being prepared for submission for publication of the material by S.W Cordaro and S.C Bott-Suzuki. The thesis author was the primary investigator and author of this material.

References

1) R. G. Forbes, "Field electron emission tutorials. I: Basic topics," 2016 Young Researchers' School in Vacuum Micro- and Nanoelectronics, Saint-Petersburg Electrotechnical University ("LETI"), October 2016.

2) O.W. Richardson. The Emission of Electricity from Hot Bodies. Longmans Green, London, 1921.

3) R.H. Fowler and L.W. Nordheim. Proc. Roy. Soc. London 119 (1928), p. 173; 124 (1929), p. 699.

4) 2 R. A. Millikan and C. C. Lauritsen, Proc. Natl. Acad. Sci. U.S.A. 14, 45 1928.

5) T. E. Stern, B. S. Gossling, and R. H. Fowler, Proc. R. Soc. London, Ser. A 124, 699 ,1929.

6) Schottky, 'Z. f. Physik,' vol. 14, p. 80 (1923).

7) J. R. Oppenheimer, Phys. Rev. 13, 66 (1928).

8) Watson, G.N (1995) " A Treatise on the Theory of Bessel Functions", Cambridge University Press.

9) Nordheim, 'Z. f. Physik,' vol. 46, p. 833 (1928).

10) A. Sommerfeld, "Zur Quantentheorie der Spektrallinien, I. Theorie der Balmerschen Serie", Ann. d. Fhys., 51 (1916), 1-44; "II. Die Feinstruktur der WasserstofF- und der wasserstoffahnlichen Linien", Ibid. (1916), 44-94; "III. Theorie der Rontgenspektren", Ibid. (1916), 125- 167.

11) Fowler, 'Roy. Soc. Proc.,' A, vol. 117, p. 549 (1928).

12) R. G. Forbes and J. H. B. Deane, Proc. R. Soc. London, Ser. A 463, 2907 2007.

13) M. Okawa, T. Shioiri, H. Okubo, S. Yanabu,"IEE Transactions on Electrical Insulation", Vol. 23,No1. 1988.

14) S. A. Slutz, M. C. Herrmann, R. A. Vesey, A. B. Sefkow, D. B. Sinars, D. C. Rovang, K. J. Peterson, M. E. Cuneo. "Pulsed-power-driven cylindrical liner implosions of laser preheated fuel magnetized with an axial field," Phys. Plasmas, vol. 17, no. 5, p. 056303, 2010.

15) R. D. McBride and S. A. Slutz Phys. Plasmas 22, 052708 (2015).

16) Williams, P. F. and Peterkin, F. E., "Triggering in trigatron spark gaps: A fundamental study" (1989). P. F. (Paul Frazer) Williams Publications. 23.

17) Byron Weber Becker, “Java: Learning to Program with Robots”, Thumbody’s Thinking Inc. 2007.

18) S. W. Cordaro, S. C. Bott-Suzuki, L. S. Caballero Bendixsen, Levon Atoyan, Tom Byvank, William Potter, B. R. Kusse, J. B. Greenly. Rev. Sci. Instrum. 86, 073503 (2015).

19) S. W. Cordaro and S. C. Bott-Suzuki J. Appl. Phys. 122, 213303 (2017)

20) S.A. Slutz, PHYSICS OF PLASMAS 17, 056303 (2010).

21) D.B. Sinars, S. A. Sultz, M. C. Herrmann, R. D. McBride, M. E. Cuneo, K. J. Peterson, R. A. Vesey, C. Nakhleh, B. E. Blue, K. Killebrew, D. Schroen, K. Tomlinson, A. D. Edens, M. R. Lopez, I. C. Smith, J. Shores, V. Bigman, G. R. Bennett, B. W. Atherton, M. Savage, W. A. Stygar, G. T. Leifeste, and J. L. Porter. Phys. Rev. Lett. (2010)

22) A.B. Sefkow, PHYSICS OF PLASMAS 21, 072711 (2014)

23) S.A. Slutz and R.A. Vesey, Phys Rev Lett (2012).

24) M.R. Gomez, S. A. Slutz, A. B. Sefkow, D. B. Sinars, K. D. Hahn, S. B. Hansen, E. C. Harding, P. F. Knapp, P. F. Schmit, C. A. Jennings, T. J. Awe, M. Geissel, D. C. Rovang, G. A. Chandler, G. W. Cooper, M. E. Cuneo, A. J. Harvey-Thompson, M. C. Herrmann, M. H. Hess, O. Johns, D. C. Lamppa, M. R. Martin, R. D. McBride, K. J. Peterson, J. L. Porter, G. K. Robertson, G. A. Rochua, C. L. Ruiz, M. E. Savage, I. C. Smith, W. A. Stygar, R. A. Vesey. Phys. Rev. Lett. 113, 155003 (2014).

25) R. G. Forbes, "Field electron emission theory (October 2016)", in: N. V. Egorov and K. A. Nikiforov (eds) Proc. 2016 Young Researchers in Vacuum Micro/Nano Electronics Conf., St Petersburg, October 2016 (Electronic ISBN 978-1-5090-4605-8) (IEEE Explore, March 2017), pp 31-39.

26) W.P. Dyke and J.K . Trolan, "The Field Emission Initiated Vacuum Arc. 11. The Resistively Heated Emitter", Phys. Rev., Vol. 91, pp. 1054-1057, 1953.

27) D. Alpert, D.A. Lee, E.M. Lyman and H.E. Tomaschke, " Initiation of Electrical Breakdown in Ultrahigh Vacuum", J. Va. Sci. andTechnol., Vol. 1, pp. 35-50, 1964.

28) A. Maitland, "New Derivation Vacuum Breakdown Equation Relating Breakdown Voltage and Electrode Separation", J. Appl. Phys., Vol.32, pp. 2399-2407, 1961.

29) L. Cranberg, "The Initiation of Electrical Breakdown in Vacuum", J. Appl. Phys., Vol. 23, pp. 518-522, 1952.

30) T. Shioiri, I. Ohshima, M. Honda, H. Okumura, H. Takahashi and H. Yoshida, "Impulse Voltage Field Emission Characteristic and Breakdown Dependency upon Field Strength in Vacuum Caps", IEEE Trans. on Power Apparatus and Systems, Vol. PAS-101, pp. 4178-4184, 1982.

31) K. Tsuruta, "Impulse Electrical Breakdown Fields of Short Vacuum Gaps", IEEE Trans. on Electrical Insulation, Vol. EI-22, pp. 77-79, 1987.

32) R. Hackam and S.K. Salman, "Effects of Electrode Curvature, Distance from Glass Insulator, and Addition of Hydrogen on Field-Emission Currents and Breakdown Voltage in Vacuum", J. Appl. Phys., Vol. 45, pp. 4384-4392, 1974.